

Syracuse University

**SURFACE**

---

Dissertations - ALL

SURFACE

---

December 2020

## 4D Printing Shape Memory Polymers for Biomedical Applications

Kathleen Pieri  
*Syracuse University*

Follow this and additional works at: <https://surface.syr.edu/etd>



Part of the [Engineering Commons](#)

---

### Recommended Citation

Pieri, Kathleen, "4D Printing Shape Memory Polymers for Biomedical Applications" (2020). *Dissertations - ALL*. 1256.

<https://surface.syr.edu/etd/1256>

This Dissertation is brought to you for free and open access by the SURFACE at SURFACE. It has been accepted for inclusion in Dissertations - ALL by an authorized administrator of SURFACE. For more information, please contact [surface@syr.edu](mailto:surface@syr.edu).

## Abstract

The development of 3D printing techniques using shape-memory polymers (SMPs) has created potentials for creating dynamic, three-dimensional structures that can be produced rapidly and be customized for specific and complex architectures. These qualities have made 3D printing a popular fabrication method for future SMP parts and devices. While important information about is known about the effects of printing parameters on 3D printed SMPs, there remains a gap in the understanding of these parameters on fundamental shape memory properties. Understanding the shape memory behavior of the SMPs post-printing can implicate potential advantages or weaknesses in using these materials in biomedical applications. Furthermore, understanding how these materials perform can lead to new advancements in platforms for cell culture, personalized medicine, and medical devices.

The primary goal of this dissertation was to evaluate a cytocompatible SMP to develop techniques to 3D print predictable substrates for biomedical applications. This was accomplished through two major aims: 1) by printing and performing material characterization of cytocompatible SMP dogbones, and 2) studying and applying programming via printing in different geometric constructs. The first part of this thesis covered the preparation of cytocompatible SMP filament and the fundamental materials characterization. The second portion addressed the development and implementation of PvP.

Chapter 2 described the process for selecting the appropriate material and developing a protocol for a printer-compatible filament for printing during the fundamental and PvP studies later in the thesis. It was determined that a commercially available SMP (SMP MM4520) would best fit the needs of the remaining experiments. A custom-made melt-spinner was chosen to produce filament from the SMP pellets.

Next, a study was carried out to evaluate the shape memory behavior of the SMP (chapter 3). While several studies have reported the effects certain parameters of the printing process has on mechanical properties or part quality, the effects of printing parameters on the shape memory abilities of the printed SMP structures is not well understood. To determine the extent to which the 3D printing process affects the fundamental shape-memory properties of a printed SMP structure, we systematically varied temperature, multiplier, and fiber orientation, that is, the direction of the individual fibers that make up the sample, and studied the effect on fixing and recovery ratios of shape-memory dogbone samples. It was found that fiber orientation significantly impacted the fixing ratio, while temperature and multiplier had little effect. No significant effects on recovery ratio were seen from any of the parameters. However, as fiber orientation went from  $0^\circ$  to  $90^\circ$ , the variability of the recovery ratios increased. These results indicate that fiber orientation is a dominant factor in the resulting shape memory capacities, specifically the fixity, of a 3D printed SMP. Further, these results suggest that the parameters have an impact on the reliability of the shape memory polymer to recover back to its original shape.

A technique for trapping strains in the SMP during printing was developed (chapter 4) for fabricating ready-to-trigger objects immediately after printing. Trapped strains were measured in 1D, 2D, and 3D samples with varied temperature, multiplier, and fiber orientation. Different geometries were observed post-triggering and simulated, and an application *in vitro* was presented in chapter 5.

4D PRINTING SHAPE MEMORY POLYMERS FOR BIOMEDICAL APPLICATIONS

by

Kathleen Pieri

B.S., Syracuse University, 2016

Dissertation

Submitted in partial fulfillment of the requirements for the degree of  
Doctor of Philosophy in Bioengineering.

Syracuse University  
December 2020

Copyright © Kathleen Pieri 2020

All Rights Reserved

*This work is dedicated to my family. Thank you for your unwavering support and encouragement.*

## Acknowledgments

First and foremost, I would like to thank my advisor, Dr. James Henderson, for his support and guidance throughout the program. To Dr. Henderson, thank you for the opportunity to have been a part of your lab and helping me transition from undergraduate to graduate life—your calmness and kindness helped me through it all. For four years I have been inspired by your dedication to both the professional and personal growth of your students, and I don't think I have ever met someone with superior time management skills.

Next, I would like to thank the members of my defense and candidacy exam committees Dr. Teng Zhang, Dr. Julie Hasenwinkel, Dr. Pranav Soman, Dr. Ma, Dr. Monroe, and Dr. Jain. I greatly appreciate their time, feedback, and enthusiasm for listening to my research projects over the past few years. Thank you to Dr. Zhang and Dr. Soman for their collaborative work and helpful insights in closely related areas of my research.

Additionally, thank you to Dr. Jeremy Gilbert, my undergraduate research and academic advisor at Syracuse University. His excitement and encouragement for pursuing a Ph.D. are what started me on this career path.

I'd like to acknowledge my lab mates and from SBI, specifically—Michelle Pede, Paul Chando, Shelby Buffington, Chenyan Wang, Plansky Hoang, and Tackla Winston. Each of them has acted as helpful co-workers, mentors, and friends when the situation called for it. Thank you to my undergraduate students Bailey Felix and Zhuoqi (Chi Chi) Tong for their hard work and perseverance in the lab, even when it got frustrating.

I would also like to acknowledge the efforts of Karen Low and Eric Finkelstein who provided assistance with managing the lab or stopping for a quick chat. And many thanks to the

BMCE department staff – Jason Markle and Amy Forbes—for their help keeping me organized with course enrollment, TA preparations, and other department business.

I would also like to thank my family. My parents, who have supported me for much longer than they ever anticipated due to my degree pursuit and proximity to home. I would not have gotten through this program without their support, and I cannot express my appreciation for all that they have done to make my life outside the lab easier. Thank you to my sister, Liz, and brother, James, who were supportive and listened to my rambling, time and time again. And thank you to my grandparents, Eleanor and Ben Ware, for always checking in on my progress with genuine interest and excitement.

Lastly, a thank you to my “Ph.D. puppy”, Bruno, whose age has served as a subtle reminder of how long I have been working towards this degree. He has endured late nights, the occasional emotional crisis, and random lab runs his entire life.

# Table of Contents

<b>List of Tables</b> .....	<b>xiii</b>
<b>List of Schemes</b> .....	<b>xiv</b>
<b>List of Figures</b> .....	<b>xvi</b>
<b>Chapter 1: Introduction</b> .....	<b>1</b>
1.1 4D printing – a fabrication method for smart materials .....	1
1.2 Shape Memory Polymers .....	2
1.3 Biomedical 4D printing with SMPs .....	4
1.4 Scope of Dissertation .....	6
1.5 References .....	10
<b>Chapter 2: Material Selection and Filament Fabrication</b> .....	<b>14</b>
2.1 Introduction and Background .....	14
2.1.1 Selection Criteria.....	14
2.1.2 Material Family: Thermoplastic Polyurethanes .....	15
2.1.3 Fabrication of TPU Filament .....	15
2.1.4 Printing .....	16
2.1.5 Characterization .....	17
2.2 Pellethane™/PCL .....	18
2.2.1 Material Information .....	18
2.2.2 Filament Fabrication.....	19

2.2.3 Printing .....	19
2.2.4 Thermal Analysis .....	20
2.3 POSS-containing Thermoplastic Polyurethane .....	20
2.3.1 Material Information .....	20
2.3.2 Filament Fabrication.....	21
2.3.3 Printing .....	22
2.3.4 Thermal Analysis .....	22
2.4 SMP MM4520.....	22
2.4.1 Material Information .....	22
2.4.2 Filament Fabrication.....	23
2.4.3 Printing .....	23
2.4 Conclusions .....	23
2.5 References .....	29
 <b>Chapter 3: Printing Parameters Affect Key Properties of 4D Printed Shape Memory</b>	
<b>Polymers .....</b>	<b>32</b>
3.1 Introduction .....	32
3.2 Methods.....	34
3.2.1 Experimental Design .....	34
3.2.2 Materials .....	35
3.2.3 Sample Preparation.....	36

3.2.4 Material Characterization .....	37
3.2.5 Statistical Analysis .....	39
3.3 Results .....	39
3.3.1 Raster Printed Samples .....	39
3.3.2 Hot Pressed Samples .....	40
3.3.3 Punched Samples .....	40
3.3.4 Printed vs Punched .....	40
3.4 Discussion .....	40
3.5 Conclusion.....	44
3.6 References .....	53
<b>Chapter 4: Programming via Printing .....</b>	<b>58</b>
4.1 Introduction .....	58
4.2 Methods.....	59
4.2.1 Experimental Design .....	59
4.2.2 Materials .....	60
4.2.3 Sample Preparation.....	60
4.2.4 Recovery and Strain Characterization .....	60
4.2.5 Modeling.....	61
3.2.6 Statistical Analysis .....	62
4.3 Results .....	62

4.3.1 Single Line Samples (1D).....	62
4.3.2 Single Layer Rectangular Samples (2D) .....	62
4.3.3 Models .....	63
4.4 Discussion .....	63
4.5 Ready-to-Trigger 4D printed SMPs using PVP .....	65
4.5.1 Sample Preparation.....	65
4.5.2 Characterization .....	66
4.5.4 Results .....	66
4.5.5 Discussion.....	67
4.6 Conclusions .....	69
4.6 References .....	81
<b>Chapter 5: Confirming Cytocompatibility and Utilizing PVP <i>in Vitro</i>.....</b>	<b>83</b>
5.1 Introduction and Background.....	83
5.2 Methods.....	84
5.2.1 Cytocompatibility of SMP MM4520 .....	84
5.2.2 Cytocompatibility of 3D Printed SMP MM4520 Using Varied Parameters .....	85
5.2.3 Distribution of Cells in SMP Scaffold Using Programming via Printing .....	85
5.2.4 Analysis and Statistics .....	86
5.3 Results.....	87
5.3.1 Cytocompatibility of SMP MM4520 .....	87

5.3.2 Cytocompatibility of 3D Printed SMP MM4520 Using Varied Parameters .....	87
5.3.3 Distribution of Cells in SMP Scaffold Using Programming via Printing .....	88
5.4 Discussion .....	89
5.4.1 Cytocompatibility of SMP MM4520 .....	89
5.4.2 Cytocompatibility of 3D Printed SMP MM4520 Using Varied Parameters .....	89
5.4.3 Distribution of Cells in SMP Scaffold Using Programming via Printing .....	90
5.5 Conclusion.....	91
5.6 References .....	96
<b>Chapter 6: Concluding Remarks and Future Work.....</b>	<b>99</b>
6.1 Overall Conclusions and Contributions .....	99
6.1.1 Material Selection and Filament Fabrication.....	99
6.1.2 Printing Parameters Affect Key Properties of 4D Printed Shape Memory Polymers.	100
6.1.3 Programming via Printing.....	100
6.1.4 Confirming Cytocompatibility and Utilizing PVP <i>in Vitro</i> .....	100
6.2 Recommendations for Future Work .....	101
6.2 References .....	102
<b>VITA.....</b>	<b>104</b>

## List of Tables

<b>Table 3-1.</b> Sample set combinations of fiber orientation, extrusion speed, and temperature printed into a type IV dogbone. ....	48
---	----

## List of Schemes

- Scheme 1-1.** Diagrams showing the main differences between 3D and 4D printing. Used with permission from F. Momeni, S. M. Mehdi Hassani, X. Liu, J. Ni, *Materials and Design*, 2017 2. Copyright © Elsevier 2017.....8
- Scheme 1-2.** Diagram showing the programming and recovery of a thermally triggered shape memory polymer. The polymer in its original, permanent, shape is heated above  $T_{\text{trans}}$  and physically deformed. It is then cooled to fix into a temporary shape, following, when desired, reheated to recover the permanent geometry. Used with permission from M. E. Pede and J. H. Henderson, *Polymer and Photonic Materials Towards Biomedical Breakthroughs*, Springer Nature. 2018<sup>8</sup>. Copyright © Springer International Publishing AG 2018. ....9
- Scheme 2-1.** A schematic for the custom-built melt-spinner which includes a (A) hollow steel barrel, (B) plunger, (C) heating cuff, (D) brass conical die with a 1.75 mm outlet, (E) polymer pellets, and (F) extruded polymer filament. ....25
- Scheme 2-2.** A schematic for the general FDM mechanism within a Makerbot 3D printer (A) thermoplastic filament, (B) drive gears, (C) heating element with nozzle, (D) deposited material layers, (E) build plate. The standard printer was modified with a custom motor mount (F) to increase the distance between the drive gears and the heating element.....26
- Scheme 3-1.** Study design overview. Following fabrication of filament by melt-spinning, dogbones are fabricated by printing, by punching from a printed sheet, or by hot-pressing. All samples were characterized using a one-way shape memory cycle (1WSMC) analysis. Fixing ratios were calculated for all samples. Recovery ratios were only calculated for 0° and 45° samples due to plastic deformation in 90° samples. ....46

**Scheme 3-2.** Raster-printed dogbone schematic showing fiber orientations. Insets: (A) raster-print edge showing continuous loops at the edge of the sample, (B) punched edge showing no loops, and (C) sample cross section showing the fiber bonding regions. For A/B and C, 0° and 90° samples are used for illustrative purposes, but the edge effects and bonding regions shown are relevant to all fiber orientations. ....47

## List of Figures

<b>Figure 2-1.</b> The chemical structure of the synthesized thermoplastic polyurethane. Used with permission from L. F. Tseng, P. T. Mather, and J. H. Henderson, <i>Acta Biomaterialia</i> , 9, 8790–8801, 20136. Copyright © Elsevier 2013.....	27
<b>Figure 2-2.</b> The general structure of the SMP MM4520. The specific structure is proprietary. Used with permission from Y. Yang, Y. Chen, Y. Wei, and Y. Li, <i>The International Journal of Advanced Manufacturing Technology</i> , 84, 2079–2095, 201613. Copyright © Springer Nature 2015.....	28
<b>Figure 3-1.</b> Images comparing (1) pre-stretching versus (2) post-stretching to show material and fiber fusion behavior of punched and raster-printed samples at 45° (A, C) and 90° (B, D) orientations. ....	49
<b>Figure 3-2.</b> Fiber orientation affects fixing ratio in both raster-printed and punched samples. Cross bars on standard deviations show group means (* $p < 0.05$ ; *** $p < 0.001$ , Tukey’s HSD post hoc). No significant effects were found for the hot-pressed control groups.....	50
<b>Figure 3-3.</b> Fiber orientation significantly affects the variance of recovery ratio of both raster-printed and punched samples. Cross bars on standard deviations show group means (* $p < 0.050$ by Bartlett’s test for raster-printed samples and F-test for punched samples). No significant effects were found for the hot-pressed control groups.....	51
<b>Figure 3-4.</b> Interactions between fiber orientation and fabrication method have a significant effect on fixing ratio for samples printed at 225°C with a multiplier of 1.0. Cross bars on standard deviations show group means (* $p < 0.05$ ; ** $p < 0.005$ ; NS $p > 0.05$ , Tukey’s HSD post hoc). ....	52

**Figure 4-1.** Temperature affects trapped strain in single line samples. Lower printing temperature led to an increase in mean trapped strain. (\*  $p < 0.05$ ; two-way ANOVA).....70

**Figure 4-2.** Representative images of the single line geometry before and after recovery when printed at temperatures of 215°C (A, C) or 225°C (B, D) with an extrusion multiplier of 1.0 (A, B) or 0.95 (C, D). .....71

**Figure 4-3.** Printing temperature affects trapped strain in 2D samples with fiber orientations of 0° (A) and 45° (B) when measured along the long axis. Temperature had no significant impact on the strain in the 90° orientation (C). (\*  $p < 0.05$ ; \*\*  $p < 0.01$ , two-way ANOVA). Note: scales on the Strain (%) axis change. ....72

**Figure 4-4.** Representative images of the free recovery behavior in 2D rectangular samples printed with varied printing parameters (printing temperature/multiplier) by row: (A) 215°C/1.0, (B)225°C /1.0, (C) 215°C /0.95, (D) 225°C /0.95. In addition to bending in the long axis, a secondary bend can be seen along the short axis, particularly in the 90° samples. ....73

**Figure 4-5.** (a) The schematic of a 1D printed fiber. (b) Gradient of the residual strain along the z-direction (normal to the printing plane). (c) A representative example of curved fiber after triggering ( $w$  is the width of the fiber). The color indicates the displacement of z-direction. Figure provided by Zhang Lab. ....74

**Figure 4-6.** (a) The schematic of a 2D printed plate with the fiber orientation as 45 degrees and thickness ( $t$ ) as 0.2 mm. (b) Deformed configurations of the plate at different levels of the residual strain. The color indicates the displacement of z-direction. Figure provided by Zhang Lab.....75

**Figure 4-7.** Representative image of the cube with three different pore sizes (small, medium, large, from bottom). All pores contracted in the direction of the fibers and the pore gradient was conserved. ....76

**Figure 4-8.** Representative image of cubes printed for cell scaffolding with (A) alternating 0° and 90°, and (B) hexagonal infill. The hexagonal infill led to a more uniform contraction upon recovery. ....77

**Figure 4-9.** Representative image of top and side views of the log pile cell scaffold. Pore size decreased dramatically after recovery, and a Poisson effect is seen in the side view. ....78

**Figure 4-10.** Representative image of the porous hinge. Top panel shows a CAD drawing of the hinge geometry. A large, downward, bending can be seen after recovery.....79

**Figure 4-11.** (a) The initial structure of a cube lattice. (b) Deformed configurations of the cube. The color indicates the displacement of x-direction. Figure provided by Zhang Lab. ....80

**Figure 5-1.** SMP MM4520 has good cytocompatibility on both substrate fabrication methods. A significant difference was found only for the substrates that were 3D printed compared to the TCPS control. (\* p < 0.05; one-way ANOVA). ....92

**Figure 5-2.** Multiplier affects viability of cells on 3D printed substrates. A lower multiplier led to a significant increase in viability at both temperature settings, but all printing parameter combinations showed high viability above 90%. (\* p < 0.05; two-way ANOVA).....93

**Figure 5-3.** Cells present in the top, middle, and bottom thirds of (A) 40°C and (C) 70°C scaffolds with corresponding total cell per field of view (B) 40°C and (D) 70°C. (\* p < 0.05; \*\* p < 0.01; \*\*\* p < 0.001, Student’s t-test).....94

**Figure 5-4.** Representative figure of x position (from left) and y position (from top) of normalized cell distribution within cross-section of (A) 40°C pre triggered (B) 40°C active, (C)

70°C pre-triggered, and (D) 70°C active scaffolds. Diamond marker shows cell position centroid.

.....95

# Chapter 1: Introduction

## 1.1 4D printing – a fabrication method for smart materials

Three-dimensional (3D) printing has become a popular fabricating method for parts and devices over the last decade. 3D printing was initially classified as a medium for rapid prototyping, where printers were used to quickly create models, prototypes, or mock-ups of a proposed device. However, due to the ability of 3D printing technology to build intricate or complex shapes, it has also been used as a primary fabrication method. The growing popularity and versatility of 3D printing have both increased and evolved the technology, and from it, a concept called 4D printing has emerged<sup>1</sup>. Simply defined, 4D printing is 3D printing a part with a time-dependent component (Scheme 1-1). This time dependency is achieved by printing with a smart material. 4D printing has enabled a way to create complex and highly tailorable smart material parts and devices<sup>2</sup>.

4D printing is a layer-by-layer additive manufacturing method for creating smart material products. The growth in research and technological advances in 4D printing has increased significantly in the past few years. It offers several advantages over traditional smart material fabrication methods including minimal waste, single-step fabrication, and precision complex architectures<sup>3</sup>. It can be classified into three groups based on feeding mechanism: liquid, powder, and solid. Liquid feed-based printers include stereolithography (SLA), digital light processing (DLP), and direct ink writing (DIW). SLA and DLP techniques use light to photopolymerize or UV cure liquid material, while DIW uses a shear-thinning ink. Powder feed systems include selective laser sintering and selective laser melting, where lasers fuse powder

particles either by solid-state or complete melting, respectively. Solid feed printers refer to fused deposition modeling, where a filament of prepared material is needed.

From above, smart materials employed in 4D printing can be solid, liquid, or powder, depending on the fabrication technique. The materials can be metallic, ceramic, polymeric, or composites. The materials have a time-dependent component, which has been generally classified as shapeshifting, such as swelling or self-repair, and shape memory materials.

4D printing has been used in several disciplines including biomedical, electronics, aerospace/automotive, and even textiles. Nadgorny et al. 4D printed a shapeshifting, pH-sensitive hydrogel valve<sup>4</sup>. The valve could be used to control flow rates at different, predetermined pH values that would cause the hydrogel to swell or shrink. Similarly, Bakarich et al. printed a thermally triggered valve that would expand in warm temperatures<sup>5</sup>. Another swelling 4D printed device was a lock-and-key actuator by Kokkinis et al. and proposed as an actuator for soft robotics<sup>6</sup>. It could also be used to lock items in place as the sides would bow out upon triggering and press against the perimeter, thus holding it in place. Zarek et al. demonstrated a 4D printed heel attachment that could change a flat shoe into a heel<sup>7</sup>.

## **1.2 Shape Memory Polymers**

Shape memory polymers (SMPs) are a class of smart material with an ability to transition from a temporary “programmed” shape, back to its original, permanent, form<sup>8</sup>. Programming is achieved through a cycle of heating, loading, cooling, and unloading. Once triggered by an external stimulus, the polymer recovers to its original shape. Stimuli can include light, water, ultrasound, enzyme, and magnetism, however, the most common triggering mechanism is heat<sup>9</sup>.

Polymers with shape-memory ability require two domains: net-points and switches. Net-points are the domain that have the highest transition temperature ( $T_{\text{trans}}$ ) and act as permanent

entanglements, or anchors, that prevent polymer flow and chain slipping during programming. The switching segment is a network that becomes flexible when it reaches a temperature above its  $T_{\text{trans}}$ , which is below that of the net-point. This can be either the segment's glass transition temperature ( $T_g$ ) or melting temperature ( $T_m$ ). Switches include amorphous polymer chains with a  $T_g$ , semi-crystalline with a  $T_m$ , or have liquid crystals with an isotropic temperature. SMPs with a  $T_g$  switch have a broad range of temperature transition, whereas those with a  $T_m$  transitioning have a sharp transition<sup>9,10</sup>. These characteristics make SMPs highly tunable.

When the SMP is heated above  $T_{\text{trans}}$ , the chains in the network become soft and flexible. When the load is added, the chains flow while the net-points remain rigid. Cooling the SMP back below  $T_{\text{trans}}$  will fix the chains in place, either through crystallization or vitrification. For thermally triggered polymers, exposure to heat re-mobilizes the chains and releases the stored strain energy, thus allowing the chains to slide back into their original position.

The versatility of the polymers and their triggering mechanisms make SMPs highly desirable for applications in biomedical devices, where the shape transition is highly advantageous in invasive surgery or tissue engineering applications due to a small starting shape and larger end shape. A few SMP devices have been approved by the U.S. Food and Drug Administration (FDA) for clinical use, with the first being a self-tying suture. This suture is made of a biodegradable block copolymer thermoplastic that is triggered by heat to close to the proper pressure for optimum wound healing<sup>11-13</sup>. Several years later, the FDA approved a thrombogenic coated SMP foam device for aneurysm treatment, which expands from heat from a laser after insertion into the abnormality<sup>14</sup>. A soft-tissue fixation device was approved for ACL treatment, which expands to anchor the ACL in place instead of screws that damage the surrounding tissues<sup>15</sup>. Other proposed devices which have been discussed and demonstrated in

the literature include vascular stents<sup>16,17</sup>, dialysis needle adaptors<sup>18</sup>, bone defect scaffolding<sup>19</sup>, and hemorrhage treatment devices<sup>20</sup>.

SMPs have also emerged as tools and platforms for biomedical research. The first reported SMP intended as a cellular research tool was from Neuss et al. They synthesized a biodegradable SMP network and studied the shape memory interactions with various cell lines to assess its aptitude for clinical applications. However, due to a triggering temperature significantly higher than body temperature, cells did not survive well on the material<sup>21</sup>. Next, the Henderson Lab developed a temperature-responsive SMP substrate that transitioned from wrinkled to smooth and studied how the change in topography could be used to direct cell behavior and morphology from aligned to random<sup>22</sup> or vice versa<sup>23</sup>. The use of SMPs as a tool to direct cells was also used by Ashby et al, who also had success and studied microarray transformations in a PCL-based SMP on controlling cell behavior<sup>24</sup>, and again by the Henderson group when an electrospun POSS thermoplastic polyurethane SMP was studied, with great success using SMPs alongside stem cells to study their mechanobiology and behavior<sup>25</sup>. Currently, SMPs have been used in active cell culture experiments to study cell motility, morphology, and differentiation.

### **1.3 Biomedical 4D printing with SMPs**

3D printing enables the production of complex and highly personalized bioinspired devices. SMPs clearly enhance the technology in biomedical applications as seen above, however, the previous examples were all prepared using traditional methods including casting, electrospinning, etc. The addition of 3D printing SMP technology has given rise to 3D scaffolds and the ability to create intricate geometries.

Targeted drug delivery has been demonstrated. Azam et al. demonstrated self-folding capsules fabricated with a biodegradable PCL using lithography to produce precision geometries such as shape, size, and porosity<sup>26</sup>. 2D templates were created using lithography of SU-8, a biocompatible, epoxy-based polymer, and hinges were made from PCL. Heat-activated the PCL hinges to self-fold the capsule. They encapsulated beads, chemical dyes, mammalian cells, and bacteria – demonstrating its diversity for drug delivery, “micro-Petri dishes”, or even pseudo-vesicles or lysosomes.

Malachowski et al. created heat-responsive drug-eluting devices comprised of a multi-fingered gripper<sup>27</sup>. A temperature sensitive hydrogel (which controls its hydrophilicity) hinge was employed to open and close the gripper, which was fabricated using photolithography. The gripper successfully grabbed tissues and could be loaded with drugs and dyes. The group then demonstrated the enhanced release of doxorubicin as compared to a control patch and released dye in the stomach of a pig. Experimental success suggested to the authors that their technology could be used as a method for sustained-release drug delivery.

Another biomedical aspect that has been demonstrated is medical devices. A stent was developed and shown as a proof of concept by Bodaghi et al. using a polyjet printer and UV cross-linked liquid photopolymer that expands when exposed to heat<sup>28</sup>. Ge et al. created a stent using high resolution micro-stereolithography and photo-curable methyl methacrylate<sup>29</sup>. Both authors used models to accurately predict the stent’s behavior.

4D printed SMPs have also been used to create cell scaffolds. Senatov et al. printed a PLA/HA scaffold and studied the effect of programming temperature on stresses formed during compression deformation and demonstrated MSC survival on a 3D printed scaffold, however, the shape memory effect was not utilized during the cell study<sup>30</sup>. Hendrikson et al. demonstrated that

4D printed SMP devices have the potential to be applied in clinical scaffolds as cells were attached and viable after recovering the sample<sup>31</sup>.

While these accomplishments are a step towards 4D advancement in biomedical applications, it should be noted that the materials and technology used in these reports are not democratized, meaning methods used to produce these materials is dependent on expensive, high resolution equipment.

## **1.4 Scope of Dissertation**

This dissertation advances 4D printing in the biomedical field. From the work presented here, recommendations can be made to improve the shape memory properties of 3D printed SMP parts. Additionally, we have explored a new process for creating ready-to-trigger parts that have been programmed during printing. This eliminates the manual programming step and also creates a way to create complex geometries that are not possible using traditional fabrication methods.

Chapter 1 (present chapter) introduces 4D printing and shape memory polymers and explains how they are currently utilized, separately and together, in the biomedical field. Chapter 2 provides the methods and selection criteria for choosing an SMP and filament making process to meet the needs of bio-applications. In chapter 3 we study the impacts of commonly employed printing parameters on the shape memory behavior of a 3D printed SMP. Chapter 4 focuses on the development of “Programming via Printing” (PvP), a process that programs the SMP during printing to eliminate the need for manual programming and create an avenue for complex shape change. Finally, in chapter 5, we study cell viability with the printed SMP material using different printing parameters, as well as a demonstration of PvP used as a cell scaffold.

The objectives of this dissertation were:

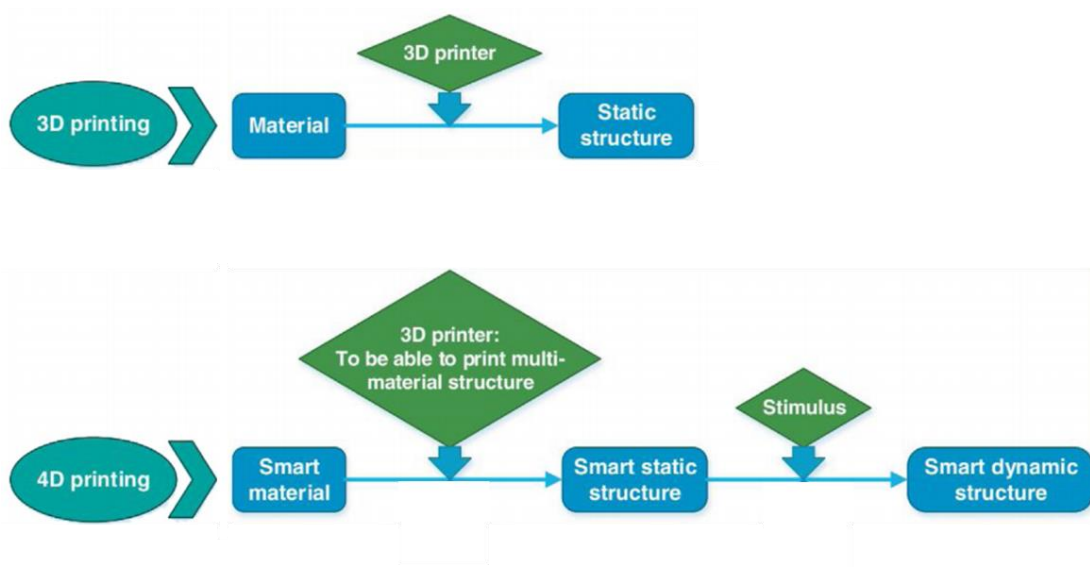
*Objective 1: Create spools of biocompatible SMPs for 3D printing.* Shape-memory polymers and extrusion-based filament fabrication methods were explored to obtain highly reproducible spools of material for printing throughout this work.

*Objective 2: Determine the extent to which printing parameters affect shape-memory behavior.* The effects of commonly incorporated printing parameters on fixing and recovery ratios were explored.

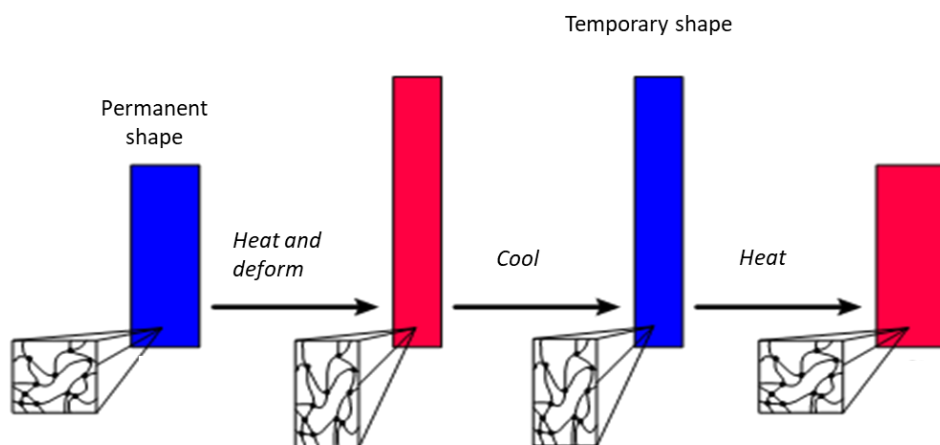
*Objective 3: Develop programming via printing to create a path for complex shape change.* Temperature and flow-rate combinations were evaluated for creating trapped strains into the material during printing for automated/complex shape changes.

*Objective 4: Determine the extent to which printing parameters affect cell viability and attachment.* Cells were seeded onto SMP samples printed with the same parameters employed in Objective 2 to analyze cell viability on 3D printed structures.

*Objective 5: Demonstrate employment of PvP in vitro.* A PvP cell scaffold was evaluated for cell distribution compared to that of static cell seeding.



**Scheme 1-1.** Diagrams showing the main differences between 3D and 4D printing. Used with permission from F. Momeni, S. M. Mehdi Hassani, X. Liu, J. Ni, *Materials and Design*, 2017 2. Copyright © Elsevier 2017.



**Scheme 1-2.** Diagram showing the programming and recovery of a thermally triggered shape memory polymer. The polymer in its original, permanent, shape is heated above  $T_{trans}$  and physically deformed. It is then cooled to fix into a temporary shape, following, when desired, reheated to recover the permanent geometry. Used with permission from M. E. Pedraza and J. H. Henderson, *Polymer and Photonic Materials Towards Biomedical Breakthroughs*, Springer Nature, 2018<sup>8</sup>. Copyright © Springer International Publishing AG 2018.

## 1.5 References

1. Tibbits, S. 4D printing: Multi-material shape change. *Archit. Des.* **84**, 116–121 (2014).
2. Momeni, F., M.Mehdi Hassani.N, S., Liu, X. & Ni, J. A review of 4D printing. *Mater. Des.* **122**, 42–79 (2017).
3. Monzón, M. D., Ortega, Z., Martínez, A. & Ortega, F. Standardization in additive manufacturing: activities carried out by international organizations and projects. *Int. J. Adv. Manuf. Technol.* **76**, 1111–1121 (2015).
4. Nadgorny, M. & Ameli, A. Functional Polymers and Nanocomposites for 3D Printing of Smart Structures and Devices. *ACS Appl. Mater. Interfaces* **10**, 17489–17507 (2018).
5. Bakarich, S. E., Gorkin III, R., Panhuis, M. in het & Spinks, G. M. 4D Printing with Mechanically Robust, Thermally Actuating Hydrogels. *Macromol. Rapid Commun.* **36**, 1211–1217 (2015).
6. Kokkinis, D. & Schaffner, M. Multimaterial Magnetically Assisted 3D Printing of Composite Materials, *Nature Communications*. (2015) doi:10.1038/ncomms9643.
7. Zarek, M. *et al.* 4D Printing Shape Memory Polymers for Dynamic Jewellery and Fashionwear. *Virtual and Physical Prototyping.* **11**, 1745-2759 (2016).
8. Pede, M. E. & Henderson, J. H., The Use of Photo-Activatable Materials for the Study of Cell Biomechanics and Mechanobiology; Polymer and Photonic Materials Towards Biomedical Breakthrough. *Springer Nature*. (2018).
9. Mather, P. T., Luo, X. & Rousseau, I. A. Shape Memory Polymer Research. *Annu. Rev. Mater. Res.* **39**, 445–471 (2009).
10. Rousseau, I. A. Challenges of Shape Memory Polymers : A Review of the Progress Toward Overcoming SMP's Limitations. *Polymer Engineering and Science*. (2008)

doi:10.1002/pen.

11. Lendlein, A. & Langer, R. Biodegradable, Elastic Shape-Memory Polymers for Potential Biomedical Applications. *Science*. **296**, 1673–1676 (2002).
12. Lendlein, A. *et al.* Shape-memory Polymers as a Technology Platform for Biomedical Applications. *Expert Rev. Med. Devices*. **7** 357-379 (2010).
13. Lendlein, A. & Langer, R. Biodegradable Shape Memory Polymer Sutures. U.S. Patent No. 10/419,323, Apr. 18, 2003.
14. Maitland, D. J. *et al.* Prototype laser-activated shape memory polymer foam device for embolic treatment of aneurysms. *Journal of Biomedical Optics*. **12**, 3–5 (2007).
15. Yakacki, C. M. *et al.* Strong, Tailored, Biocompatible Shape-Memory Polymer Networks. *Adv. Funct. Mater.* **18**, 2428–2435 (2008).
16. Yakacki, C. M. *et al.* Unconstrained recovery characterization of shape-memory polymer networks for cardiovascular applications. *Biomaterials* **28**, 2255–2263 (2007).
17. Baer, G. M. *et al.* Fabrication and in vitro deployment of a laser-activated shape memory polymer vascular stent. *BioMedical Engineering OnLine*. **8**, 1–8 (2007).
18. Ortega, J. M. *et al.* A Shape Memory Polymer Dialysis Needle Adapter for the Reduction of Hemodynamic Stress Within Arteriovenous Grafts. *IEEE Transactions on Biomedical Engineering*. **54**, 1722–1724 (2007).
19. Baker, R. M., Tseng, L.-F., Iannolo, M. T., Oest, M. E. & Henderson, J. H. Self-deploying shape memory polymer scaffolds for grafting and stabilizing complex bone defects: A mouse femoral segmental defect study. *Biomaterials* **76**, 388–398 (2016).
20. Monroe, M. B. B. *et al.* Multifunctional Shape-Memory Polymer Foams with Bio-inspired Antimicrobials. *ChemPhysChem* **19**, 1999–2008 (2018).

21. Neuss, S. *et al.* The use of a shape-memory poly( $\epsilon$ -caprolactone)dimethacrylate network as a tissue engineering scaffold. *Biomaterials* **30**, 1697–1705 (2009).
22. Davis, K. A., Luo, X., Mather, P. T. & Henderson, J. H. Shape Memory Polymers for Active Cell Culture. *J. Vis. Exp.* 2–6 (2011) doi:10.3791/2903.
23. Yang, P., Baker, R. M., Henderson, J. H. & Mather, P. T. Soft Matter dynamically aligns adherent cells. *Soft Matter*. **9**, 4705–4714 (2013) doi:10.1039/c3sm00024a.
24. Le, D. M., Kulangara, K., Adler, A. F., Leong, K. W. & Ashby, V. S. Dynamic Topographical Control of Mesenchymal Stem Cells by Culture on Responsive Poly ( $\epsilon$  - caprolactone ) Surfaces. *Adv. Mater.* **23**, 3278–3283 (2011) doi:10.1002/adma.201100821.
25. Tseng, L. F., Mather, P. T. & Henderson, J. H. Shape-memory-actuated change in scaffold fiber alignment directs stem cell morphology. *Acta Biomater.* **9**, 8790–8801 (2013).
26. Azam, A., Laflin, K. E., Jamal, M., Fernandes, R. & Gracias, D. H. Self-folding micropatterned polymeric containers. *Biomed Devices*. **13**, 51–58 (2011) doi:10.1007/s10544-010-9470-x.
27. Malachowski, K. *et al.* Stimuli-Responsive Theragrippers for Chemomechanical Controlled Release. *Angew. Chem. Int. Ed.* **53**, 8045–8049 (2014) doi:10.1002/anie.201311047.
28. Bodaghi, M., Damanpack, A. R. & Liao, W. H. Self-expanding/shrinking structures by 4D printing. *Smart Mater. Struct.* **25** (2016).
29. Ge, Q. *et al.* Multimaterial 4D Printing with Tailorable Shape Memory Polymers. *Sci. Rep.* **6**, 1–12 (2016).
30. Senatov, F. S. *et al.* Shape memory effect in 3D-printed scaffolds for self-fitting implants. *Eur. Polym. J.* **93**, 222–231 (2017).

31. Hendrikson, W. J. *et al.* Towards 4D printed scaffolds for tissue engineering: Exploiting 3D shape memory polymers to deliver time-controlled stimulus on cultured cells. *Biofabrication* **9**, (2017).

## **Chapter 2: Material Selection and Filament Fabrication**

### **2.1 Introduction and Background**

Smart materials used in 4D printing are chosen based on factors such as need, performance, and printer compatibility. In this work, we used an FDM printer and a shape memory polymer (SMP) to create 4D printed objects. Section 2.1 explains how an appropriate SMP was chosen for our experiments and gives an overview of the methods for making filament, printing, and material characterization. Specific protocols for these methods are discussed for each SMP in sections 2.2-2.4.

#### **2.1.1 Selection Criteria**

The work in this dissertation is intended to advance 4D printing in biomedical applications, and consequently, several material attributes—cytocompatibility, process-ability, and printability—needed to be considered when selecting an appropriate SMP for our experiments. Proposed applications for 4D printed biomedical devices include cell culture platforms and scaffolds, where the material will come into direct contact with cells or tissues. Therefore, an appropriate SMP candidate for these biomedical applications must have low cytotoxicity and suitable cell attachment. In addition to cytocompatibility, the SMP must be able to be reliably processed into a filament with the proper 1.75mm diameter to fit our FDM printer, and that filament must print consistently without causing jams or defects in the printed object. Finally, because of the repeated heating and cooling necessary to create the filament and deposit it during printing, the SMP must be resistant to heat degradation and not breakdown due to cycling above and below its melt temperature.

### **2.1.2 Material Family: Thermoplastic Polyurethanes**

Thermoplastic polyurethanes (TPUs) are versatile polymers that can be customized for their intended purpose, which made them an ideal class of SMP for our proposed work. A TPU is synthesized from an isocyanate and an alcohol to create a urethane bond and each component can be modified to alter the properties of the material. Isocyanate segments can be aliphatic or aromatic, aliphatic TPU medical devices have demonstrated UV resistance and in-body softening, while aromatic TPUs have good chemical resistance<sup>1,2</sup>. The backbone composition of the alcohol can be a polyester, or polyether. TPUs with polyester-based alcohols are susceptible to hydrolytic attack, and will degrade inside the body, making them ideal materials for biodegrading devices. In contrast, polyether-based TPUs are resistant to both hydrolysis and oxidation, which make them suitable for long-term devices or in contact with blood<sup>3</sup>.

To further tailor the TPU properties, the percentages of isocyanate versus alcohol segments can be adjusted, thus making TPUs highly versatile and suitable for processing, while also having strength and flexibility. In our study, three TPUs with previously demonstrated shape memory properties and cytocompatibility: Pellethane<sup>TM</sup>/PCL blend<sup>4</sup>, POSS-based<sup>5,6</sup>, and commercially available SMP pellets<sup>7</sup>, were chosen to be evaluated for 4D printing.

### **2.1.3 Fabrication of TPU Filament**

Methods for creating filament out of different amounts of raw SMPs had to be developed in order to use the materials successfully in a 3D printer. While a polymer extruder is suitable for making filament from large quantities (>25 grams) of polymer pellets, current methods for extruding small amounts of material have not been reported. This severely limits 4D printing development with SMPs that are synthesized in research labs and yield small batches of non-uniform (i.e. non-pellet) products.

#### *2.1.3.1 Melt-Spinner*

To accommodate material feeds less than 20 grams, an existing custom-built melt-spinner was used<sup>8</sup>. The melt-spinner is a mechanical extrusion device that consists of a barrel, heating cuff, plunger, die, spooler, and a thermocouple feedback system (Scheme 2-1). The melt-spinner plunger and spooler are controlled through DMC Terminal using G-code, and the temperature of the heating cuff is independently set by the user.

To extrude filament, SMP is added to the barrel, which is heated by the heating cuff until melted. The SMP melt is extruded out of the die at the end of the barrel by lowering the plunger and is collected on a spool to maintain a constant diameter. Specific protocols for the SMPs are described in sections 2.3.2 and 2.4.2.

#### *2.1.3.2 Extruder*

A single-screw extruder (Microtruder RCP-0625, Randcastle Extrusion Systems, Inc.), hereafter as “Extruder”, was used to make filament when quantities >20 grams of polymer pellets were available. A custom dye with a 1.75mm outlet was made to match the diameter required by the 3D printer feed mechanism. The Extruder has four heating zones: 1, 2, 3, and die, with a thermocouple feedback in each. The screw drives the polymer pellets through the heating zones and out the die. Specific protocols for the SMPs are described in sections 2.2.2 and 2.4.2.

### **2.1.4 Printing**

A MakerBot® Replicator™ 2X was used for all 3D printing. Like all FDM printers, the MakerBot® feeds material to its nozzle by drive wheels, which grip and push the solid filament through the heating element and out the nozzle (Scheme 2-3). In this model, the drive wheels and heating element are in close proximity, and due to the low transition temperatures of the SMPs, heat conduction from the printer’s heating element through the filament often causes jamming.

This happens when the filament softens and is unable to be pushed into the nozzle. Instead, the now-rubbery filament wraps around the drive wheels. To remedy this, we designed and 3D printed a motor-mount with an opening for airflow (Scheme 2-3(F)). It was placed between the drive wheels and the heating element to create enough distance and additional cooling so that the filament remained below  $T_g$  and could be pushed through the nozzle.

Each SMP was tested in the printer to determine which material printed most reliably. Temperature ranges for which the SMP flowed fully out of the nozzle were established for each material. Temperatures below the range prevented material flow out of the nozzle, and temperatures above the range caused the material to bubble or “foam” out of the nozzle. Both conditions prevented adequate material deposition and consequently created defects in each printed layer. Specific protocols for each SMP are described in sections 2.2.3, 2.3.3, and 2.4.3.

## **2.1.5 Characterization**

### *2.1.2.1 Thermal Analysis*

Each SMP was characterized by thermal analysis. Thermal analysis consisted of TGA to find the degradation temperatures of each material, which was taken when 99% of the mass remained after heating the material to 600°C at 10°C per minute. DSC was run to confirm the transition temperatures of each SMP. Additionally, differential scanning calorimetry (DSC) was performed on SMP filament and print samples to determine if the filament fabrication or printing processes effected the thermal properties due to the continuous heat cycling. Two cycles of heating and cooling were run on the DSC, and the data was analyzed from the second cycle. All thermal analysis data was analyzed using TA Universal Analysis software.

### 2.1.2.2 Quality Analysis

Filament quality is a vital component to successful FDM printing. The filament must have a diameter that fits the printer and must also be consistent. Ahmed et al. reported that consistent filament diameter was the most important element of the filament. The filament should also be solid and smooth with no air bubbles<sup>9</sup>. Air bubbles are a problem for two major reasons. First, it creates gaps in the material, so there is inconsistent flow out of the nozzle, which creates defects in the print. Second, bubbles expand when subjected to high temperatures, which expands the local diameter of the filament. This can result in jamming or filament breakage. The SMP filaments were visually inspected for smoothness and bubbles. The diameters were measured with calipers and threaded through a spare printer extruder to check for diameter consistency.

## 2.2 Pellethane™/PCL

### 2.2.1 Material information

A 50:50 wt% blend of a Pellethane™ (5380-80A, Lubrizol Corporation) and Poly-ε-caprolactone (PCL) was chosen because of its demonstrated fixing, recovery, and cytocompatibility<sup>4</sup>. It was also chosen because of its easy fabrication method which required melt-mixing (*see section 2.2.2*) the two components together rather than synthesis. As a blended SMP, the thermal triggering occurs at the PCL melting temperature while Pellethane™ serves as net-points. This particular Pellethane™ is an elastomer comprised of an aromatic isocyanate and a poly-ether alcohol with a  $T_g$  of  $-37^\circ\text{C}$  and a  $T_m$  of  $135^\circ\text{C}$ . PCL ( $M_n = 80,000$ ) is a semi crystalline polymer with a  $T_m$  of  $64^\circ\text{C}$  and has been widely used commercially and in biomedical research due to its biocompatibility and versatile physical and mechanical properties when blended with other polymers<sup>10-12</sup>.

### **2.2.2 Filament Fabrication**

The Extruder was used to melt-mix and extrude the Pellethane™/PCL blend into filament in a single step. We did not use the melt-spinner because the heat and plunge extrusion mechanism did not mix the Pellethane™ and the PCL together in a uniform filament of material. A 50:50 mix of Pellethane™ and PCL was made by adding 15g of each polymer to the Extruder's hopper. The zones were set to 170°C, 180°C, 185°C, 190°C, respectively, based on the extrusion recommendations from Lubrizol for Pellethane™. These temperatures were below the PCL thermal degradation temperature of 280°C and did not cause any accidental material loss.

Both Pellethane™ and PCL are above  $T_g$  at room temperature, which resulted in a rubbery and flexible filament. It was discovered that humidity greatly affected the quality of the extrusion process. On dry days, the resulting filament was smooth, well mixed with no portion containing only one of the polymers, and had a consistent diameter (1.76 mm +/- 0.04). In contrast, filament extruded on high humidity days was unsuitable for printing because it contained bubbles and portions with only one polymer.

### **2.2.3 Printing**

The Pellethane™/PCL blend could be printed between 195°C and 215°C, with the best printing flow at 205°C. Even with the printer modifications, the flexible filament often wrapped around the drive wheels and jammed the printer. Additionally, the filament would often stick to the inside of the nozzle, start to burn, and cause a clog. Flexible filaments are reportedly difficult to print, and issues we observed, were likely due the inability of the drive wheels to push soft filament into the heating element<sup>13</sup>.

## 2.2.4 Thermal Analysis

The degradation temperature of the Pellethane™/PCL blend was found to be 260°C by TGA. Samples of the filament and printed Pellethane™/PCL blend were evaluated using DSC to determine the  $T_g$  of the polymer. A cycle of heating at 10°C/min to 200°C followed by cooling 10°C/min to 0°C was run twice for each sample. The  $T_g$  of the filament and printed material was found to be 61°C and 62°C, respectively.

## 2.3 POSS-containing Thermoplastic Polyurethane

### 2.3.1 Material information

A shape-memory, thermoplastic polyurethane was developed by the Henderson and Mather Labs containing polyester and POSS components (Figure 2-1). This TPU is biodegradable and cytocompatible with POSS serving as net-points. Both labs have successfully used this TPU *in vivo* as a method for healing bone defects and *in vitro*<sup>5,6,14</sup>.

TPU was synthesized in a two-step reaction: the synthesis of a polyol with a target molecular weight ( $M_n$ ) of 12,000 g/mol and a subsequent reaction with Hexamethylene diisocyanate (HDI) (Sigma-Aldrich, 52649) to link 1,2-propanDiolIsobutyl POSS (Hybrid Plastics, AL0130) to the polyol. The synthesis developed by Tseng, et al. was followed and described below<sup>6</sup>.

D,L –lactide ((3,6-Dimethyl-1,4-dioxane-2,5-dione, LA monomer, Sigma-Aldrich, 303143) was dissolved in ethyl acetate (Fisher Scientific, E145-500) and crashed out for purification. To link the monomer together, 1,4-Butandiol (Sigma-Aldrich, 240559) and Tin(II) 2-ethylhexanoate (Sigma-Aldrich, S3252) were added to the lactide and left to react at 140C for 12 hours under nitrogen. Tetrahydrofuran (THF) (Fisher Scientific, T-400) was added to the flask to dissolve the polyol and precipitated out in hexanes (Fisher Scientific, H-292), then dried for three days.

Polyurethane was synthesized with the dry polyol and POSS (Hybrid Plastics, AL0130). The polyol was dissolved in distilled toluene (Fisher Scientific, T-290). HDI and a few drops of Dibutyltin dilaurate (Sigma-Aldrich, 291234) were added to the dissolved polyol under nitrogen. POSS was added after 30 minutes and the temperature was increased to 90°C. Extra HDI was added to the reaction every hour for 5 hours to improve the molecular weight of the TPU, which ideally is 200,000 g/mol. The reaction was left to run for 24 hours after the final HDI addition. Finally, the TPU was precipitated out in cold hexanes and left to dry for at least three days. Proper synthesis yields a polymer with a  $T_g$  near body temperature, making it a physiological relevant material at the biological interface. Small batches of 10-15 grams of material achieved the target  $M_n$  compared to larger batches (>20 grams).

### **2.3.2 Filament Fabrication**

The melt-spinner was used to fabricate filament from the synthesized TPU, which yielded an average of 12 grams of filament. It should be noted that TPU batches exceeding 350,000 g/mol could not be extruded due to its lack of flow when heated. Before making filament, the plunger, barrel, and die were flame dried and stored in a vacuum oven at 80°C overnight. To make filament, the die was heated on a hotplate to 120°C. TPU was added to the inside of the die and packed in to help eliminate air bubbles. The die was then screwed onto the end of the barrel, and filled with more TPU. The heating cuff was placed around the barrel and set to 120°C. As the TPU inside the barrel became rubbery, it was pushed down and compacted using the plunger, and then more TPU was added. This was repeated until the barrel was filled with heat-packed TPU and greatly eliminated air bubbles during extrusion. The plunger is lowered using g-code through DMC Terminal and the polymer flows out of the die and is collected on the spooler.

Similar to the Pellethane™/PCL blend, the filament extrusion process was sensitive to humidity. Under dry conditions, the filament extruded smooth with little to no bubbles. The

filament was stiff and brittle, which made it difficult to be stored for later use. On humid days the filament would bubble or foam out of the melt-spinner and produce inconsistent filament, which could not be used for printing.

### **2.3.3 Printing**

The TPU was printed the most reliably at 120°C, and had a narrow printing range from 118°C -122°C. Filament jamming was not common, however, clogs in the nozzle would occur for prints lasting longer than 2 minutes, due to overheating and degradation of the material inside the nozzle.

### **2.3.4 Thermal Analysis**

DSC was used to determine the  $T_g$  of the raw polymer, filament and prints. A cycle of heating at 10°C/min to 140°C followed by cooling 10°C/min to 0°C was run twice for each sample. The  $T_g$  of the raw SMP, filament, and prints were all near 56°C (around 36°C wet). The heating cycles for making the filament and printing did not affect the  $T_g$  of the material.

## **2.4 SMP MM4520**

### **2.4.1 Material information**

A commercially available SMP was also evaluated for use in our experiments. SMP MM4520, a thermoplastic polyurethane elastomer was purchased in pellet form from SMP Technologies Inc (Figure 2-2). It has a polyether backbone and is semi crystalline<sup>13,15</sup>, with a  $T_m$  of 200°C and  $T_g$  of 45°C. SMP MM4520 is part of a tailored  $T_g$  line synthesized by SMP Technologies Inc, with other  $T_g$ s of 35°C, 55°C, and 65°C available. We chose this particular SMP family because of its triggering temperature near body temperature, and its demonstrated cytocompatibility<sup>7,16-18</sup> and success in previous 4D printing work<sup>13,19-22</sup>. Additional studies were carried out to confirm cell viability with MM4520 in Chapter 5.

### **2.4.2 Filament Fabrication**

The SMP MM4520 filament was prepared using both the Extruder and the melt-spinner. The Extruder's zones were set to 180°C, 190°C, 205°C, 210°C respectively. These temperatures were used based on guidelines provided by the manufacturer, and also Yang et al, who explored the different extruder temperature settings and how it affected the quality of the filament<sup>13</sup>.

The melt-spinner was also used to make small batches of filament. The hot plate and heat cuff were set to 200°C, and the heat-packing procedure described above was followed. The material was extruded at 200°C and collected on the spooler for use.

### **2.4.3 Printing**

This SMP could be printed between 205°C and 230°C. No nozzle clogging occurred, and jamming was rare – only occurring in the upper temperature range during long prints (>5min).

### **2.4.4 Thermal Analysis**

DSC was used to determine the  $T_g$  of the polymer pellets, filament, and prints. A cycle of heating at 10°C/min to 250°C followed by cooling 10°C/min to 0°C was run twice for each sample. The  $T_g$  of the SMP pellets, filament, and prints were all 46°C, indicating the heating cycles for making the filament and printing did not affect the  $T_g$  of the material. DSC was also used to confirm the  $T_g$  of the material after exposure to 37°C water for 24 hours. This analysis showed a plasticizing effect of water on the SMP, which lowered the  $T_g$  to about 30°C, which is consistent with what has been reported in the literature<sup>10</sup>.

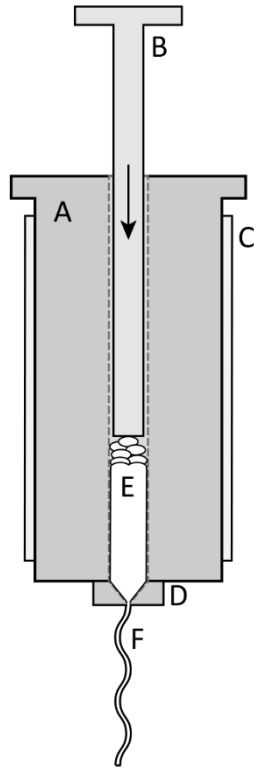
## **2.4 Conclusions**

Three SMPs were evaluated in this chapter for their potential implementation in the remaining studies. The Pellethane™/PCL blend was considered unsuitable because of its difficulty during printing. The material would clog and cause jamming due to the high flexibility of the filament. The POSS-based TPU was determined to be unfit for printing for several

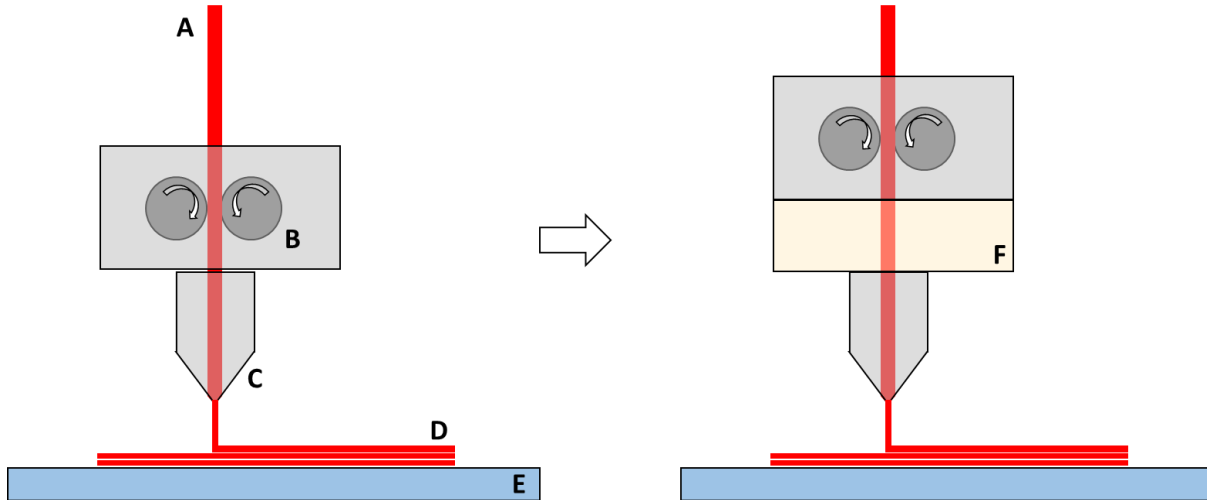
reasons. First, synthesis of the TPU took about two weeks and often over- or undershot its target molecular weight, making it unable to be extruded. The TPU was also difficult to extrude when it was humid, and the lab environment does not have an adequate mechanism for constant humidity control. Lastly, the TPU filaments were very brittle and could not be “spooled”. Sticks of filament were used and were limited to approximately 40 cm. This limited the volume of the object that could be printed.

The most reliable material and method was determined to be the SMP MM4520 filament fabricated with the Extruder. This filament diameter was the most consistent, contained the least amount of bubbles and could be made in large quantities in short periods of time. It also printed the most reliably and at a largest range of temperatures and appeared to be the most resistant to changes in humidity. For the remaining studies in this dissertation, SMP MM4520 was used.

*Additional acknowledgements for this chapter:* Michelle Pede and Shelby Buffington for their guidance in polymer synthesis techniques, Peter Lok and Lucas Albrect for their assistance with preliminary 3D printing, and Prof. Monroe and Changling Du for their support with supplemental SMP characterization.



**Scheme 2-1.** A schematic for the custom-built melt-spinner which includes: (A) hollow steel barrel, (B) plunger, (C) heating cuff, (D) brass conical die with a 1.75 mm outlet, (E) polymer pellets, and (F) extruded polymer filament.



**Scheme 2-2.** A schematic for the general FDM mechanism within a Makerbot 3D printer (A) thermoplastic filament, (B) drive gears, (C) heating element with nozzle, (D) deposited material layers, (E) build plate. The standard printer was modified with a custom motor mount (F) to increase the distance between the drive gears and the heating element.

*Thermoplastic polyurethane chemical structure*

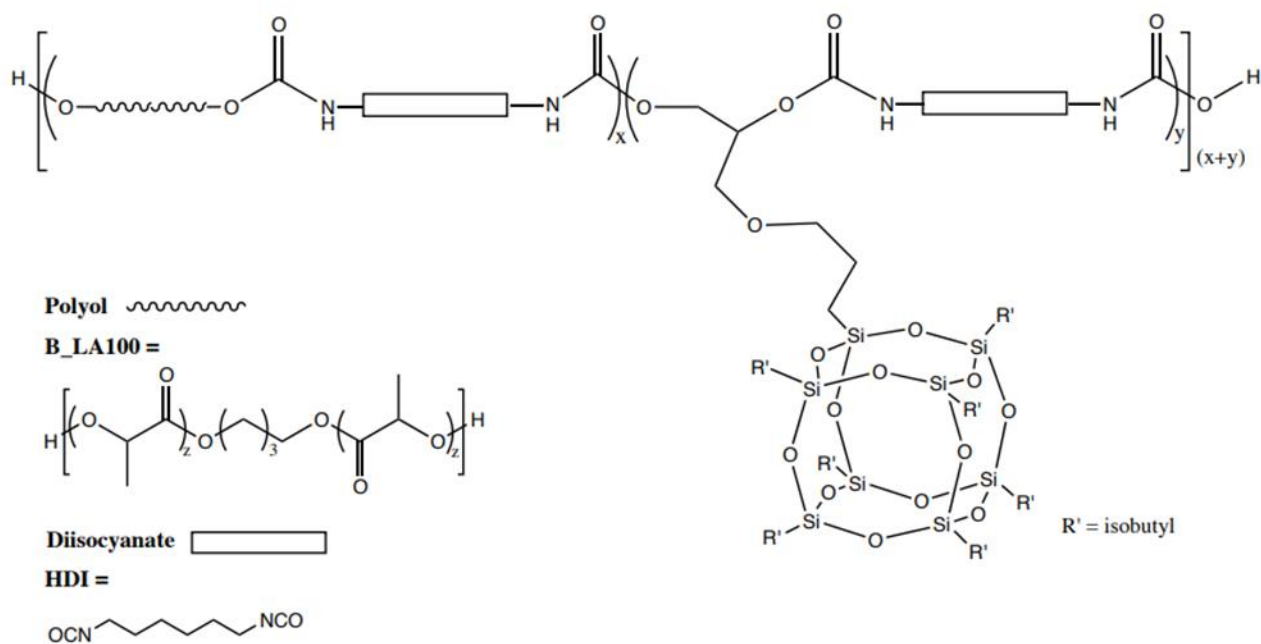


**Figure 2-1.** The chemical structure of the synthesized thermoplastic polyurethane. Used with permission from L. F. Tseng, P. T. Mather, and J. H. Henderson, *Acta Biomaterialia*, 9, 8790–8801, 20136. Copyright © Elsevier 2013.

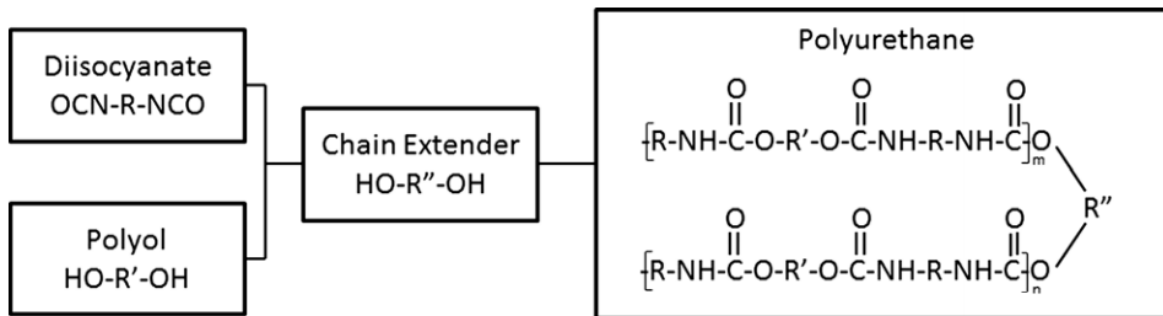


**Figure 2-2.** The general structure of the SMP MM4520. The specific structure is proprietary.

Used with permission from Y. Yang, Y. Chen, Y. Wei, and Y. Li, The International Journal of Advanced Manufacturing Technology, 84, 2079–2095, 201613. Copyright © Springer Nature 2015.

## 2.5 References

1. Rousseau, I. A. Challenges of Shape Memory Polymers : A Review of the Progress Toward Overcoming SMP's Limitations. *Polymer Engineering and Science*. (2008) doi:10.1002/pen
2. González-Henríquez, C. M., Sarabia-Vallejos, M. A. & Rodríguez-Hernandez, J. Polymers for additive manufacturing and 4D-printing: Materials, methodologies, and biomedical applications. *Progress in Polymer Science* vol. 94 57–116 (2019).
3. Soldani, G. *et al.* Long term performance of small-diameter vascular grafts made of a poly(ether)urethane–polydimethylsiloxane semi-interpenetrating polymeric network. *Biomaterials* **31**, 2592–2605 (2010).
4. Buffington, S. L. *et al.* Enzymatically triggered shape memory polymers. *Acta Biomater.* **84**, 88–97 (2019).
5. Baker, R. M., Tseng, L.-F., Iannolo, M. T., Oest, M. E. & Henderson, J. H. Self-deploying shape memory polymer scaffolds for grafting and stabilizing complex bone defects: A mouse femoral segmental defect study. *Biomaterials* **76**, 388–398 (2016).
6. Tseng, L. F., Mather, P. T. & Henderson, J. H. Shape-memory-actuated change in scaffold fiber alignment directs stem cell morphology. *Acta Biomater.* **9**, 8790–8801 (2013).
7. Farè, S. *et al.* In vitro interaction of human fibroblasts and platelets with a shape-memory polyurethane. *J. Biomed. Mater. Res. - Part A* **73**, 1–11 (2005).
8. Ouellette, E. S. Novel Methods and Self-Reinforced Composite Materials for Assessment and Prevention of Mechanically Assisted Corrosion in Modular Tapers. (2016).
9. Ahmed, O., Hasan, S. & Lal, J. Optimization of fused deposition modeling process parameters for dimensional accuracy using I-optimality criterion. *Measurement* **81**, 174–

- 196 (2016).
10. Garces, I. T., Aslanzadeh, S., Boluk, Y. & Ayranci, C. Effect of moisture on shape memory polyurethane polymers for extrusion-based additive manufacturing. *Materials (Basel)*. **12**, (2019).
  11. Gong, T. *et al.* The Control of Mesenchymal Stem Cell Differentiation Using Dynamically Tunable Surface Microgrooves. *Adv. Healthc. Mater.* **3**, 1608–1619 (2014).
  12. Huang, G. *et al.* Functional and Biomimetic Materials for Engineering of the Three-Dimensional Cell Microenvironment. *Chem. Rev.* **117**, 12764–12850 (2017).
  13. Yang, Y., Chen, Y., Wei, Y. & Li, Y. 3D printing of shape memory polymer for functional part fabrication. *Int. J. Adv. Manuf. Technol.* **84**, 2079–2095 (2016).
  14. Wang, J. *et al.* Shape memory activation can affect cell seeding of shape memory polymer scaffolds designed for tissue engineering and regenerative medicine. *J. Mater. Sci. Mater. Med.* **28**, 1–9 (2017).
  15. Shunichi Hayashi. Shape Memory Polyurethane Elastomer. U.S. Patent No. 5,145, 35 (1992).
  16. De Nardo, L. *et al.* Preparation and characterization of shape memory polymer scaffolds via solvent casting/particulate leaching. *J. Appl. Biomater. Funct. Mater.* **10**, 119–126 (2012).
  17. De Nardo, L. *et al.* Shape memory polymer foams for cerebral aneurysm repair: Effects of plasma sterilization on physical properties and cytocompatibility. *Acta Biomater.* **5**, 1508–1518 (2009).
  18. Metcalfe, A. *et al.* Cold hibernated elastic memory foams for endovascular interventions. *Biomaterials* **24**, 491–497 (2003).

19. Garcia Rosales, C. A. *et al.* Characterization of shape memory polymer parts fabricated using material extrusion 3D printing technique. *Rapid Prototyp. J.* **25**, 322–331 (2019).
20. Abuzaid, W., Alkhader, M. & Omari, M. Experimental analysis of heterogeneous shape recovery in 4d printed honeycomb structures. *Polym. Test.* **68**, 100–109 (2018).
21. Hendrikson, W. J. *et al.* Towards 4D printed scaffolds for tissue engineering: Exploiting 3D shape memory polymers to deliver time-controlled stimulus on cultured cells. *Biofabrication* **9**, (2017).
22. Hu, G. F., Damanpack, A. R., Bodaghi, M. & Liao, W. H. Increasing dimension of structures by 4D printing shape memory polymers via fused deposition modeling. *Smart Mater. Struct.* **26**, (2017).
23. Randcastle Extrusion Systems Inc. Randcastle’s Microtruders. U.S. Patent No. 5,486,328

# Chapter 3: Printing Parameters Affect Key Properties of 4D Printed Shape Memory Polymers

## 3.1 Introduction

Fused filament fabrication (FFF) is a widely used method of additive manufacturing that enables 3D printing of complex parts using a continuous thermoplastic filament. The filament is heated to its melting temperature and deposited in layers to print the part from the bottom up. The print path is created using slicing software from computer-aided design (CAD) drawings, which, in combination with the deposition process, results in an efficient and low-cost method for building complex part architectures<sup>1</sup>. The accessibility of FFF technology for both researchers and consumers has enabled 3D printing to be used not only as a method of rapid prototyping but also as a method of primary fabrication of new parts.

FFF is one of several methods that have been employed in the development of 4D printing—the 3D printing of smart materials—wherein the dynamic, time-dependent functionality of the smart material provides the “fourth” dimension<sup>2,3</sup>. 4D printing produces structures with the capacity to change form or function when triggered by an external stimulus<sup>4</sup>. The stimulus can be physical (such as heat<sup>5,6</sup>), electrical<sup>7,8</sup>, or even biochemical<sup>9</sup>. Structures produced through 3D printing can be complex and highly tailorable, making 4D printing a useful fabrication option for parts made from smart materials. FFF was chosen for our study because it is the most widely used and most easily democratized compared to other technologies (e.g. Polyjet, DLP)<sup>10</sup>.

Shape memory polymers (SMPs) are materials of growing interest for 4D printing. Because of their comparatively low processing temperatures and costs, when compared to shape

memory alloys (SMAs), and capacity for shape-changing functionality, when compared to composites, SMPs have potential advantages over other smart materials for many applications. SMPs are a class of smart material with the ability to remember an original shape, be deformed and fixed into a temporary shape, and later return to the original shape when triggered by an external stimulus. To program an SMP, the polymer is first heated above its transition temperature ( $T_{\text{trans}}$ ), for example, glass transition temperature ( $T_g$ ) or melting temperature ( $T_m$ ), and configured into a new, temporary shape. The polymer is then cooled back below  $T_{\text{trans}}$  to immobilize the polymer chains and store the strain energy within the geometry through vitrification or crystallization. To recover the SMP back to the original shape, an external stimulus (e.g., heat<sup>5,6,11-13</sup>) is applied, which remobilizes the polymer chains and releases the strain. The shape memory effect is commonly quantified in terms of shape fixing and shape recovery ratios: the fixing ratio characterizing the ability of an SMP to hold its temporary shape; and the recovery ratio characterizing the ability to return to its original, permanent shape. These measures are critical in the understanding of the functionality of SMP structures.

Although several studies have examined the extent to which the parameters of the 3D printing process affect physical properties<sup>14-16</sup> and quality<sup>15,17</sup> of printed SMP parts, fundamental questions as to the effect of 3D printing on shape memory behavior remain. Villacres et al. found that printing angle and infill percentage significantly impact ultimate tensile stress, elastic modulus, and maximum strain<sup>14</sup>. Yang et al. studied the effect of processing parameters on part density, dimensional accuracy, and surface roughness, intending to improve SMP part quality<sup>15</sup>. Abuzaid et al. studied the relationship between fiber orientation and shape change to understand part shrinkage<sup>17</sup>. Rosales et al. looked at the effect of print speed, layer height, and print temperature on Young's modulus, fixing ratio, and recovery ratio<sup>16</sup>. While that study found that

higher temperatures, higher layer heights, and lower speeds led to a higher Young's modulus, the findings for fixing and recovery ratios were only reported for samples printed using a single set of parameters (temperature, speed, and layer height of 235°C, 100 mm/s, and 0.25 mm, respectively) and were affected by the amount of strain programmed into the sample during testing. The investigation into fixing and recovery was additionally limited by the programming conditions, which were carried out at room temperature (below  $T_g$ ), and the short recovery time near  $T_g$ , (45°C and 50°C for 1 min each), leading to an unclear demonstration of the impact of the printing parameters. Thus, prior investigations have established that printing speeds and temperatures can affect physical properties and part quality, yet the extent to which the 3D printing process affects shape memory behavior, including shape fixing and recovery, remains under-examined and poorly understood. Until such understanding is achieved, accurate design, precise high-fidelity printing, and reproducible shape memory actuation of 3D printed SMP parts are unlikely to be realized.

Here, our goal was to determine the effect of the printing process on shape memory behavior. To achieve this, three critical and commonly controlled printing parameters—temperature, extrusion rate multiplier, and fiber orientation—were systematically varied when printing dogbone samples, and the effect of the parameters on shape memory behavior was quantified by measuring shape fixing and recovery.

## **3.2 Methods**

### **3.2.1 Experimental Design**

To investigate the extent to which printing parameters affect fixing and recovery, dogbone samples were produced using systematically varied nozzle temperature, extrusion multiplier, and fiber orientation (Scheme 3-1). Each parameter was statistically analyzed as a

categorical factor (e.g., “high” and “low”) and not a numerical value in case of inaccuracies in the printer resolution (e.g., small deviations in the programmed flow rate, temperature, or fiber orientation).

To control for multiplier and fiber orientation effects, additional dogbone samples were punched from hot-pressed SMP sheets. To control for the effect of material looped at the sample edge from one line to the next during raster printing, dogbones were also punched from a printed SMP sheet. Fixing and recovery ratios for each sample were calculated after conducting a one-way shape memory cycle (1WSMC) using a dynamic mechanical analyzer (DMA). Comparisons between fixing ratios and between recovery ratios were made within each printed and punched group to determine the effect of printing parameters, within each hot-pressed group to determine the effect of temperature, and between the printed and punched groups to determine the effect of raster-printed edges.

### **3.2.2 Materials**

Commercially available semi-crystalline thermoplastic polyurethane pellets (MM-4520, SMP Technologies Inc., Japan) were used for all experiments. This SMP is aromatic with a polyether backbone with a  $T_g$  of 45°C and melting temperature ( $T_m$ ) of ~200°C and was chosen for this study because of its demonstrated success with fused filament 3D printers<sup>15,16,18</sup>.

Modifications were made to a Makerbot Replicator 2X (Makerbot® Industries, LLC) to prevent printer jamming due to heat conduction from the heating element through the SMP filament, which becomes rubbery and wraps around the printer’s extruder drive gears – inhibiting deposition. To remedy this, a motor mount was added to create more distance between the drive gears and the heating element. To further reduce head conductance, an air tube was placed in the motor mount to direct airflow over the filament, similar to a design described by Yang et al.<sup>15</sup>.

### 3.2.3 Sample Preparation

#### 3.2.3.1 Raster Printed Samples

Dogbones were designed by CAD (Autodesk Inventor, Autodesk, USA, 2019) to comply with the ASTM dogbone type IV standard, scaled down by a factor of 4. Temperature, extrusion rate multiplier, and fiber orientation were varied for each sample set. In this paper, we define nozzle temperature as the temperature the heating element located in the printer's extruder is set to during printing. Extrusion multiplier controls the volume of polymer extrusion relative to nozzle translational velocity. Fiber orientation is the direction the material is deposited during printing, with 0° defined in the present study as the long axis of the dogbone and 90° corresponding to the width. Preliminary printing was conducted to determine the range of printing parameters that produced samples of sufficient quality, which we defined as a lack of bubbles, gaps, or defects in the object upon visual inspection<sup>19</sup>. Based on the preliminary printing evaluation, the following printing parameters were chosen for the study. The printing temperatures used were 215°C and 225°C, with an intentional separation of ten degrees to prevent an overlap in printing temperature due to over- or undershot nozzle heating. Extrusion multipliers used were 0.95 and 1.0, and the fiber orientations used were 0°, 45°, and 90° (Scheme 3-2A; Figure 3-1A, B). Systematically varying the printing parameters yielded twelve sample sets (Table 3-1). The infill was set to 100%, and each layer in a sample was printed using the same parameters. The print bed was set to 25°C and the printing speed was held constant at 3600 mm/s. All dogbones were printed in a batch of three samples (with the same parameters) in the same place on the print bed in case of non-uniform heating. The samples were left to cool on the print bed before removal.

### 3.2.3.2 Hot-Pressed Samples

To control for fiber orientation and multiplier, we created samples of homogenous material (i.e., no fibers) by hot-pressing SMP filament into films. To fabricate these control samples, filament from the melt-spinner was placed between two sheets of Teflon with a 0.60 mm spacer and inserted between two heated plates of a benchtop hydraulic press (Carver 3851-0, USA) at 215°C or 225°C. The filament was pressed stepwise at 0.25 tons per 5 minutes to eliminate air bubbles, then held at 1 ton until cool. Pressure was released and dogbones were punched from the resulting film using a type IV dogbone punch with the same dimensions as the printed dogbones.

### 3.2.3.3 Punched Samples

To determine if raster print edge effects play a role in fixing or recovery, dogbone samples were also punched from a large printed sheet (Scheme 3-2B; Figure 3-1C, D). To fabricate these control samples, a rectangular sheet was printed at 225°C with a multiplier of 1.0 while all other printer settings were kept as described above. The sheet was printed in the same place on the print bed as the raster-printed dogbones. From the printed sheet, dogbones were punched out using the same method as the hot-pressed samples. Samples possessing the three different fiber orientations being studied were achieved by rotating the punch on the sheet to 0°, 45°, and 90°, relative to the fiber direction of the printed sheet.

## 3.2.4 Material Characterization

Fixing and recovery ratios were calculated after performing a 1WSMC using DMA. The 1WSMC is a thermomechanical cycling of an SMP<sup>20</sup>, wherein the SMP is heated above its  $T_{\text{trans}}$  to a rubbery state, then deformed under stress to a predetermined strain. The force is held constant as the SMP is cooled back below  $T_{\text{trans}}$  to fix the polymer chains. The sample is

unloaded, and the temperature is increased above  $T_{\text{trans}}$ , triggering the release of the stored strain energy as the SMP recovers<sup>20</sup>. The strains measured before and after deformation, after unloading, and after recovery can be used to determine the fixing and recovery ratios.

Samples were loaded into the DMA and, using a force-controlled sequence, heated above  $T_g$  to 90°C, isothermally held for 10 minutes to ensure uniform heating, and then stretched at 0.02 N/min to elongate the samples to 20% of their initial length. Upon reaching 20% strain the temperature was decreased to 0°C to fix the sample in the strained state. The sample was then heated back to 90°C at 2.0°C/min and held isothermally at 90°C for 10 min to completely recover the sample. This cycle was repeated four times and the strains from cycles two through four were used to calculate fixing ratio and recovery ratio. For the punched dogbones, which were more sensitive to applied stresses, 0.001 N/min was used during the stretching portion of the cycle to prevent programmed strain from overshooting 20% of their initial length.

#### 3.2.4.1 Fixing Ratio and Recovery Ratio

Fixing ratio was calculated as

$$R_f(\%) = \frac{\varepsilon_u(N)}{\varepsilon_m(N)} \times 100$$

and recovery ratio calculated as

$$R_r(\%) = \frac{\varepsilon_u(N) - \varepsilon_p(N)}{\varepsilon_u(N) - \varepsilon_p(N-1)} \times 100,$$

where  $\varepsilon_u$  is strain after unloading,  $\varepsilon_m$  is the strain after deformation, and  $\varepsilon_p$  is the permanent strain following recovery<sup>20,21</sup>. Ideal shape memory behavior is considered  $R_f = R_r = 100\%$ , and while the specific application of an SMP tends to determine what constitutes a sufficient fixing ratio or recovery ratio, generally close to 100% is considered favorable and necessary<sup>20</sup>. Values greater than 100% are possible for both fixing and recovery ratios and indicate expansion of the

material during fixing and recovery past the original length, respectively. Both effects can be caused by changes in crystalline alignment during solid-state phase transformation of the polymer chains when heated and cooled<sup>22</sup>. Fixing ratios of 100% indicate that an SMP has perfect fixing and maintains its exact temporary shape.

### 3.2.5 Statistical Analysis

Three independent samples were prepared and tested for all conditions (n=3). All comparisons were made using the R statistical analysis software (R Core Team, 2019). One-way ANOVA was performed with Tukey's HSD for multiple comparison testing, and a two-way ANOVA was performed for comparisons with multiple variables. Temperature, multiplier, and fiber orientation data were analyzed as categorical factors. Means were considered statistically different for  $p < 0.05$ . Bartlett's test or F-test was used to determine equal variance. Reported p-values are from ANOVA unless otherwise indicated and p-values between two factors are indicated with a subscript (e.g. "p<sub>t,m</sub>" denotes p-value for interactions between temperature and multiplier, "p<sub>0°,45°</sub>" denotes p-value of fiber orientation levels comparing 0° and 45°).

## 3.3 Results

### 3.3.1 Raster Printed Samples

For the raster printed dogbone samples, fiber orientation had a significant effect on fixing ratio ( $p = 4.03 \times 10^{-9}$ ) but no significant effect was found for temperature ( $p = 0.42$ ), or any interactions ( $p_{t,m} = 0.72$ ,  $p_{t,f} = 0.56$ ,  $p_{m,f} = 0.22$ ). All fiber orientations were statistically different from one another ( $p_{0°,45°} = 0.02$ ,  $p_{0°,90°} = 1.0 \times 10^{-6}$ ,  $p_{90°,45°} = 2.0 \times 10^{-6}$ , Tukey's HSD; Figure 3-2). Additionally, increasing the degree of fiber orientation from 0° to 45° and to 90° resulted in a significant increase in the distribution of recovery ratio values ( $p_{0°,45°} = 6.6 \times 10^{-4}$ ,  $p_{0°,90°} = 5.3 \times 10^{-7}$ ,  $p_{90°,45°} = 0.01$ , Bartlett's test; Figure 3-4).

### 3.3.2 Hot Pressed Samples

Consistent with our findings from the printed samples, temperature had no significant effect on fixing ratio ( $p = 0.98$ ) or recovery ratio ( $p = 0.089$ ).

### 3.3.3 Punched Samples

For punched samples, which control for raster printed edges, fiber orientation had a significant effect on fixing ratio ( $p = 0.004$ ). Fixing ratios for  $0^\circ$  and  $90^\circ$  samples were statistically different from each other, as were those for  $0^\circ$  and  $45^\circ$  ( $p_{0^\circ,45^\circ} = 0.005$ ,  $p_{0^\circ,90^\circ} = 0.01$ , Tukey's HSD). Fiber orientations of  $90^\circ$  did not recover after programming, therefore recovery ratios could not be reported for those samples (see *Discussion*). The variance of recovery ratio values for  $0^\circ$  and  $45^\circ$  samples were significantly different ( $p_{0^\circ,45^\circ} = 1.67 \times 10^{-5}$ , F-test).

### 3.3.4 Printed vs Punched

There was a significant interaction between the effects of fiber orientation and fabrication method on fixing ratio ( $p = 0.01$ ; Figure 3-5), where orientations of  $0^\circ$  and  $90^\circ$  showed no significant effect from fabrication method but there was a significant effect at  $45^\circ$  ( $p_{\text{punch, r-print}} = 0.004$ , Tukey's HSD). When the fiber orientation was  $45^\circ$ , there was a statistical difference between the  $0^\circ$  and  $45^\circ$  orientations that were punched ( $p_{0^\circ,45^\circ} = 0.0003$ , Tukey's HSD), which does not appear when the samples were raster-printed ( $p_{0^\circ,45^\circ} = 0.55$ , Tukey's HSD). Differences in recovery ratio were not statistically significant for any of the printing parameters.

## 3.4 Discussion

The results reveal that printing parameters used in FFF can affect key shape memory properties of 3D printed SMPs. In raster printed samples, the fiber orientation was found to affect mean fixing ratio, but not mean recovery ratio, while temperature and multiplier did not significantly affect either ratio. The data showed that when strain direction was aligned with fiber direction (i.e., the  $0^\circ$  orientation), the average fixing ratio approached 100% ( $99.45 \pm$

1.8%). At 45°, fixing ratio was consistently in the upper 90% range with an average of 98%. The 90° orientation had a less consistent fixing ratio and a range of 92–98%. While the mean recovery ratios were not statistically different for each fiber orientation, the data showed a trend of increasing variability in recovery ratio as the orientation increased from 0° to 90°. This suggests that fiber orientation may affect the reliability of the shape memory behavior of a printed SMP.

Similar trends were found in the punched sample data, which revealed a fiber orientation effect on fixing ratio. Unlike the raster printed samples, there was no significant difference between 45° and 90° fiber orientation for fixing. Also, punched samples at 90° orientations did not recover once programmed during the one-way shape memory cycle. This suggests that the edge behavior of the raster print path contributes to the overall behavior of the shape memory sample. Additional support for this speculation was seen in the comparisons between the punched and the raster-printed samples that were fabricated at 225°C and a multiplier of 1.0. Considering fixing ratio, when printed the 45° orientation had shape memory behavior similar to the printed 0° orientation, but when punched had shape memory behavior similar to that of the punched 90° orientation.

Fiber orientation also affected the distribution of recovery ratios for both the raster-printed and punched samples. For example, in the raster printed dogbones, 0° samples had recovery ratios ranging from 90-98%, 45° samples ranging from 85-102%, and 90° samples ranging from <80-104%. The standard deviation of each recovery ratio was significantly different than all others. The same trend is seen in the samples that were punched, where the 0° orientations had values tightly clustered around 95%, while the 45° orientation had a range from <10-109%. These findings suggest that fiber orientation can affect the distribution of recovery

ratio values and contribute to less reliable shape memory behavior when the fiber orientation is not aligned with the loading direction.

A possible reason for why we see the trend in fiber orientation may be the mechanical deformation of the fusion regions between fibers. Bellehumeur et al. described these fusions as sintering or semi-molten coalescence of printed fibers<sup>23</sup>. They found that the strength of the bonding is highly dependent on printing temperature and that higher temperatures led to stronger bonding and greater contact area. However, they found that the fibers cool too rapidly to ensure complete bonding, and therefore the properties of the bonding region are different from those of the fibers. In the present study, as fiber orientation increased to 90°, fibers became less aligned with the loading direction as applied during shape memory programming in the DMA.

Therefore, at the higher angles, the strain increasingly occurred not only in the fiber but also in the width of the fusion points between fibers. If mechanical properties are weaker in the fusion region compared to the width of the fibers due to incomplete bonding and a smaller cross-sectional area<sup>23,24</sup> (Scheme 3-2C), the effects of fiber orientation observed in our study could be explained by plastic deformation in the bonding regions. As fiber orientation increases to 90°, plastic deformation in the bonding regions would affect the ability of the sample to remain fixed and to recover, due to local material damage including chain disentanglement<sup>21</sup> and micro-cracks<sup>25</sup>. The extra material that is laid down in a raster-printed edge could stabilize the 45° and 90° samples because the additional loop of material stretches in the direction of strain and reduces the concentration of stress in the bonding regions. This lessens the severity of the plastic deformation of the material in the bonding regions, which would allow better fixing and recovery of the SMP. This has implications regarding the size of the printed object. For example, had our

study used a larger dogbone, the size of the loops relative to the dimensions of the sample cross-section would be smaller, which would presumably diminish the edge effects.

Temperature, multiplier, and fiber orientation are among the most common user-adjusted print settings, and in order to produce high fidelity SMP parts via 4D printing, it is critical to understand how even a small change in setting might impact shape memory behavior. Polymers can be printed within a range of temperatures and our preliminary studies revealed the SMP used in this work can be printed as low as 210°C and as high as 230°C. As printing temperatures approach the low end of the range, the molten polymer becomes increasingly viscous and leads to nozzle clogging. On the other hand, the high end of the range causes both bubbles in the extruded fiber and material degradation. Temperatures of 215°C and 225°C were chosen because both are well within the printing range and have enough separation to prevent any over or under-shooting (a consequence from the sensitivity of the printer's temperature sensor) of the temperature from overlapping, or falling outside of the printing range. The small temperature range for this particular SMP deemed the analysis of additional temperatures unnecessary.

The extrusion multiplier parameter controls the material flow rate and adjusts the volume of polymer extruded from the nozzle per unit time. Multiplier has been shown to influence the porosity of 3D printed objects and is commonly adjusted for part quality purposes. In most FFF 3D printers, including the MakerBot used in this work, the flow rate is automatically calibrated by the printing software to ensure adequate material extrusion for the travel speed specified by the user<sup>19</sup>. An increase or decrease in multiplier will increase or decrease the rotation speed of the feed gears, respectively. For our SMP we used 1.0 (printer default equal to the calculated gear rotation speed), and 0.95, (95% of the calculated gear rotation speed).

As the popularity of employing SMPs for basic science<sup>26–30</sup> and biomedical applications<sup>31–34</sup> grows, and as 3D printing of SMPs grows simultaneously<sup>35–37</sup>, the ability to precisely control the shape memory behavior of a printed SMP part is crucial. For example, the potential exists for implementing SMPs in applications such as minimally invasive surgery, where laparoscopes place small SMP devices which are then expanded to a larger, permanent form once positioned<sup>5</sup>. However, printing parameters during fabrication could render a device ineffective or even dangerous to patients if a 3D printed cardiovascular stent<sup>38</sup> was to only partially, or not reliably, recover—thereby not opening the vessel. The inability to hold a temporary shape would be equally detrimental, as the stent could start expanding in the body before reaching the deployment site. 3D printed SMP bone anchor device would have similar challenges, where poor fixing and unreliable recovery would prevent a proper fit<sup>39</sup>.

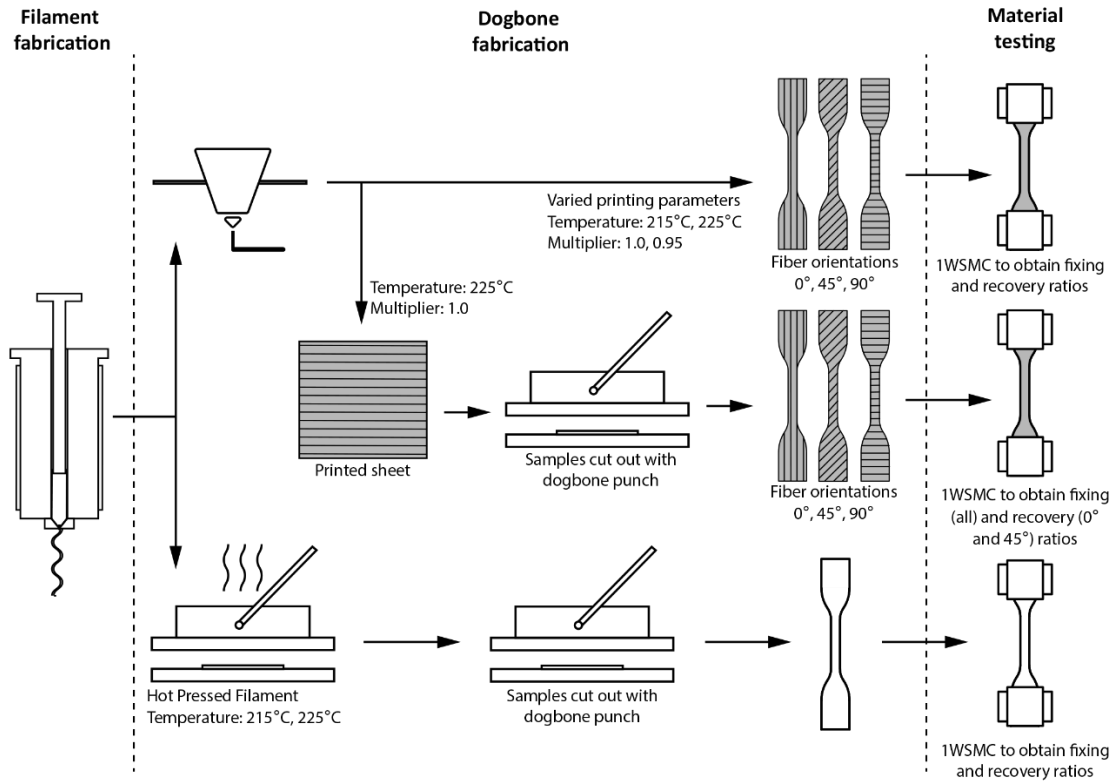
The 4D printing field is growing rapidly, and investigations of 4D printed SMPs beyond the fundamental considerations in this work include studies to evaluate printing parameters' effect on pre-strain in the printed SMP<sup>18,40</sup>. The pre-strain is used as a programming mechanism for the SMP during printing and has the potential to create self-morphing objects and parts. Before such advancement can be regularly implemented in the field, we must have a robust understanding of how the parameters impact the shape memory behavior of printed objects. Here, we have provided insight into the effects of printing parameters using commercially available SMP and FFF technology, and our findings suggest that other available 4D printing technology should be similarly evaluated.

### **3.5 Conclusion**

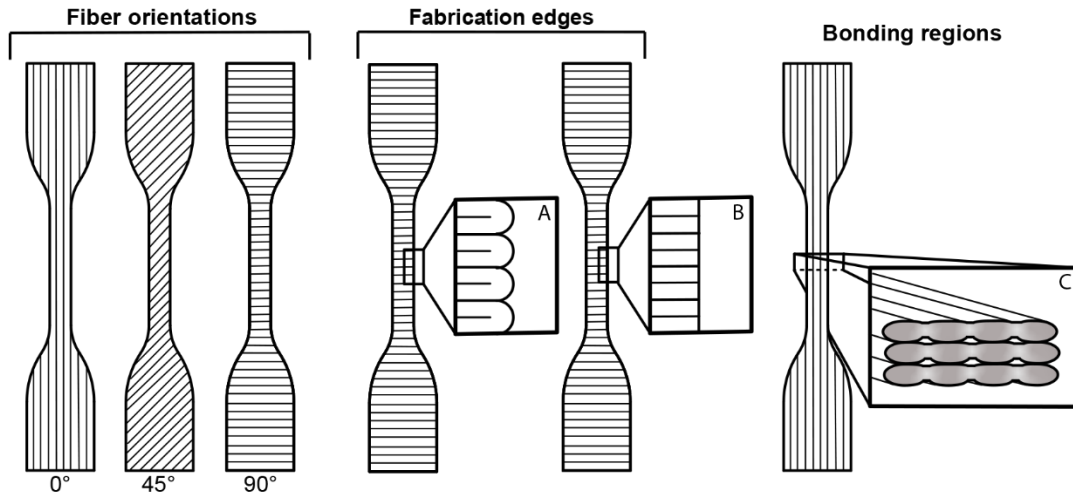
This study demonstrated the impact of printing parameters on the shape memory behavior of 3D printed SMPs. We found that fiber orientation has the most significant effect on shape

memory properties, where an increase in fiber orientation from 0° to 90° decreases the fixing ratio and increases the variance in recovery ratios, likely due to local plastic deformations of the bonding regions between fibers. These findings indicate it is essential to carefully plan the print path of a 3D printed SMP part so that the fibers orient optimally with the direction of programmed strain for the prescribed application. Failure to do so could result in poor fixing and recovery, resulting in an SMP device with a questionable ability to perform its intended function.

*Additional acknowledgements for this chapter:* Paul Chando, for his expertise in 3D printing technology; Bailey Felix for her help with data acquisition; James Pieri, for his assistance with computer aided design.



**Scheme 3-1.** Study design overview. Following fabrication of filament by melt-spinning, dogbones are fabricated by printing, by punching from a printed sheet, or by hot-pressing. All samples were characterized using a one-way shape memory cycle (1WSMC) analysis. Fixing ratios were calculated for all samples. Recovery ratios were only calculated for 0° and 45° samples due to plastic deformation in 90° samples.



**Scheme 3-2.** Raster-printed dogbone schematic showing fiber orientations. Insets: (A) raster-print edge showing continuous loops at the edge of the sample, (B) punched edge showing no loops, and (C) sample cross section showing the fiber bonding regions. For A/B and C, 0° and 90° samples are used for illustrative purposes, but the edge effects and bonding regions shown are relevant to all fiber orientations.

<b>Table 1: Raster-printed parameters</b>		
<b>Fiber Orientation (° to long axis)</b>	<b>Extrusion Rate (Multiplier)</b>	<b>Print Temperature (°C)</b>
0	0.95	215
		225
	1.0	215
		225
45	0.95	215
		225
	1.0	215
		225
90	0.95	215
		225
	1.0	215
		225

**Table 3-1.** Sample set combinations of fiber orientation, extrusion speed, and temperature printed into a type IV dogbone.

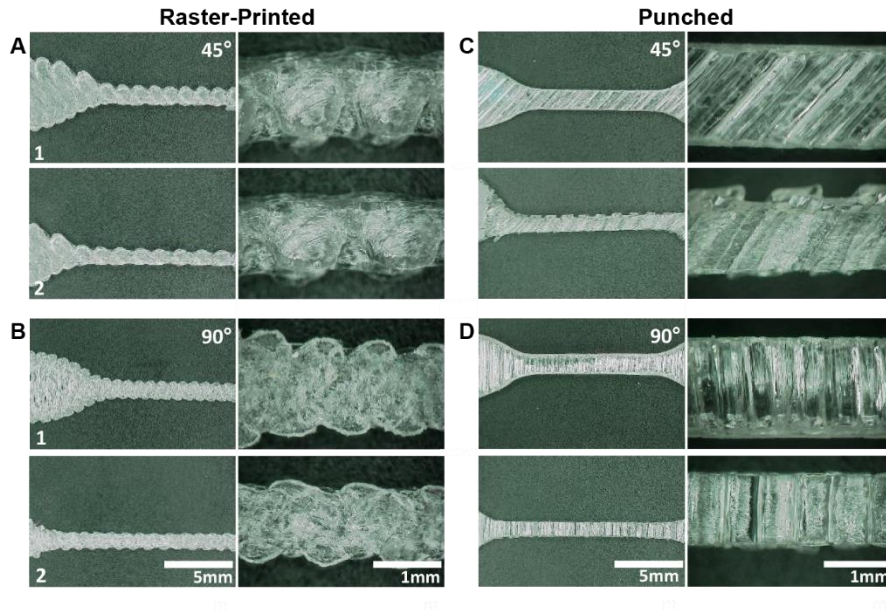


**Figure 3-1.** Images comparing (1) pre-stretching versus (2) post-stretching to show material and fiber fusion behavior of punched and raster-printed samples at 45° (A, C) and 90° (B, D) orientations.

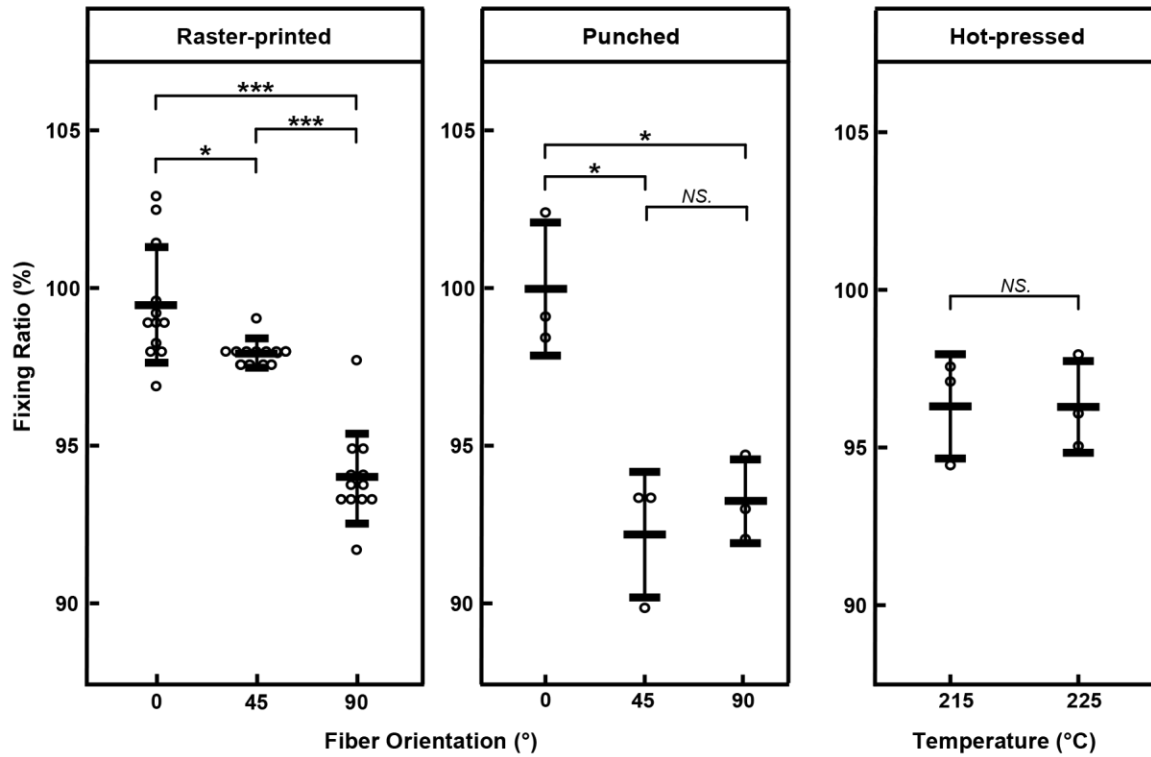


**Figure 3-2.** Fiber orientation affects fixing ratio in both raster-printed and punched samples.

Cross bars on standard deviations show group means (\*  $p < 0.05$ ; \*\*\*  $p < 0.001$ , Tukey's HSD post hoc). No significant effects were found for the hot-pressed control groups.

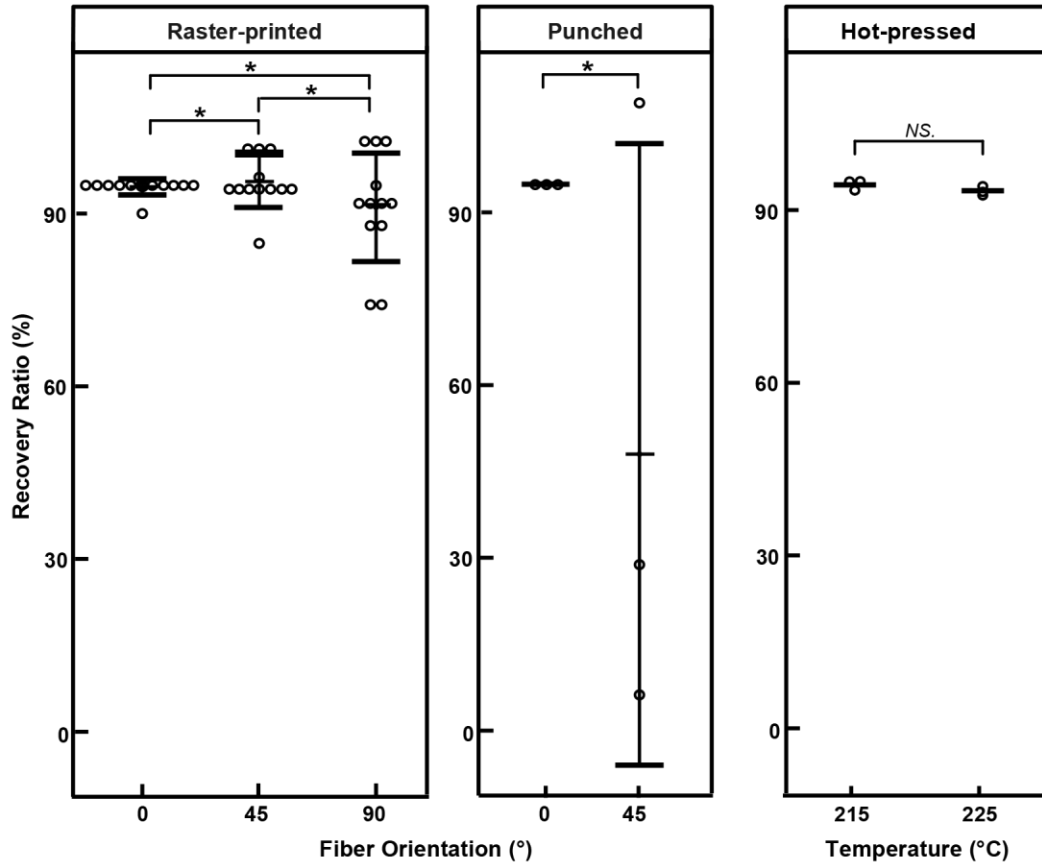


**Figure 3-3.** Fiber orientation significantly affects the variance of recovery ratio of both raster-printed and punched samples. Cross bars on standard deviations show group means (\*  $p < 0.050$  by Bartlett's test for raster-printed samples and F-test for punched samples). No significant effects were found for the hot-pressed control groups.

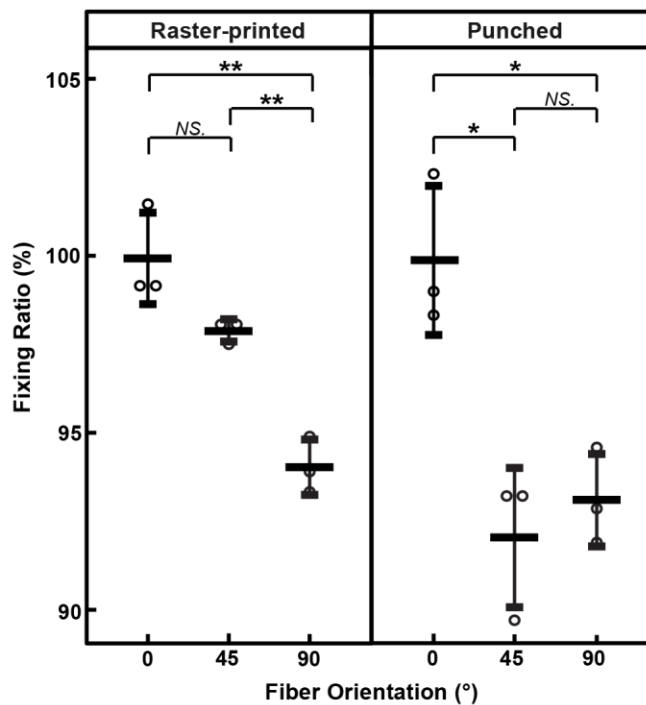


**Figure 3-4.** Interactions between fiber orientation and fabrication method have a significant effect on fixing ratio for samples printed at 225°C with a multiplier of 1.0. Cross bars on standard deviations show group means (\*  $p < 0.05$ ; \*\*  $p < 0.005$ ; NS  $p > 0.05$ , Tukey’s HSD post hoc).

### 3.6 References

1. Rastogi, P. & Kandasubramanian, B. Breakthrough in the printing tactics for stimuli-responsive materials : 4D printing. *Chem. Eng. J.* **366**, 264–304 (2019).
2. Tibbits, S. 4D printing: Multi-material shape change. *Archit. Des.* **84**, 116–121 (2014).
3. Momeni, F., M.Mehdi Hassani, N, S., Liu, X. & Ni, J. A review of 4D printing. *Mater. Des.* **122**, 42–79 (2017).
4. Choi, J., Kwon, O.-C., Jo, W., Lee, H. J. & Moon, M.-W. 4D Printing Technology: A Review. *3D Print. Addit. Manuf.* **2**, 159–167 (2015).
5. Lendlein, A. & Langer, R. Biodegradable, Elastic Shape-Memory Polymers for Potential Biomedical Applications. *Science (80-. )*. **296**, 1673–1676 (2002).
6. Baker, R. M., Henderson, J. H. & Mather, P. T. Shape memory poly( $\epsilon$ -caprolactone)-copoly(ethylene glycol) foams with body temperature triggering and two-way actuation. *J. Mater. Chem. B* **1**, 4916–4920 (2013).
7. Koerner, H., Price, G., Pearce, N. A., Alexander, M. & Vaia, R. A. Remotely actuated polymer nanocomposites—stress-recovery of carbon-nanotube-filled thermoplastic elastomers. *Nat. Mater.* **3**, 115 (2004).
8. Sahoo, N. G., Jung, Y. C. & Cho, J. W. Electroactive shape memory effect of polyurethane composites filled with carbon nanotubes and conducting polymer. *Mater. Manuf. Process.* **22**, 419–423 (2007).
9. Buffington, S. L. *et al.* Enzymatically triggered shape memory polymers. *Acta Biomater.* **84**, 88–97 (2019).
10. Statista. Most used 3D printing technologies in 2020. (2020).
11. Davis, K. A., Luo, X., Mather, P. T. & Henderson, J. H. Shape Memory Polymers for

- Active Cell Culture. *J. Vis. Exp.* 2–6 (2011) doi:10.3791/2903.
12. Tseng, L. F., Mather, P. T. & Henderson, J. H. Shape-memory-actuated change in scaffold fiber alignment directs stem cell morphology. *Acta Biomater.* **9**, 8790–8801 (2013).
  13. Baker, R. M., Tseng, L.-F., Iannolo, M. T., Oest, M. E. & Henderson, J. H. Self-deploying shape memory polymer scaffolds for grafting and stabilizing complex bone defects: A mouse femoral segmental defect study. *Biomaterials* **76**, 388–398 (2016).
  14. Villacres, J., Nobes, D. & Ayranci, C. Additive manufacturing of shape memory polymers: effects of print orientation and infill percentage on mechanical properties. *Rapid Prototyp. J.* **24**, 744–751 (2018).
  15. Yang, Y., Chen, Y., Wei, Y. & Li, Y. 3D printing of shape memory polymer for functional part fabrication. *Int. J. Adv. Manuf. Technol.* **84**, 2079–2095 (2016).
  16. Garcia Rosales, C. A. *et al.* Characterization of shape memory polymer parts fabricated using material extrusion 3D printing technique. *Rapid Prototyp. J.* **25**, 322–331 (2019).
  17. Abuzaid, W., Alkhader, M. & Omari, M. Experimental analysis of heterogeneous shape recovery in 4d printed honeycomb structures. *Polym. Test.* **68**, 100–109 (2018).
  18. Bodaghi, M., Damanpack, A. R. & Liao, W. H. Adaptive metamaterials by functionally graded 4D printing. *Mater. Des.* **135**, 26–36 (2017).
  19. Gordeev, E. G., Galushko, A. S. & Ananikov, V. P. Improvement of quality of 3D printed objects by elimination of microscopic structural defects in fused deposition modeling. (2018).
  20. Mather, P. T., Luo, X. & Rousseau, I. A. Shape Memory Polymer Research. *Annu. Rev. Mater. Res.* **39**, 445–471 (2009).
  21. Rousseau, I. A. Challenges of Shape Memory Polymers : A Review of the Progress

- Toward Overcoming SMP's Limitations. *Polymer Engineering and Science*. (2008)  
doi:10.1002/pen
22. Jang, B. Z. & Zhang, Z. J. Thermally- and phase transformation-induced volume changes of polymers for actuator applications. *J. Intell. Mater. Syst. Struct.* **5**, 758–763 (1994).
  23. Bellehumeur, C., Li, L., Qian, S. & Peihua, G. Modeling of Bond Formation Between Polymer Filaments in the Fused Deposition Modeling Process. *J. Manuf. Process.* **6**, 170–178 (2004).
  24. Li, L. An analysis and fabrication of FDM prototypes with locally controlled properties. (University of Calgary, 2002).
  25. Shojaei, A., Li, G. & Voyiadjis, G. Z. Cyclic viscoplastic-viscodamage analysis of shape memory polymers fibers with application to self-healing smart materials. *J. Appl. Mech. Trans. ASME* **80**, 1–15 (2013).
  26. Wang, J., Quach, A., Brasch, M. E., Turner, C. E. & Henderson, J. H. On-command on / off switching of progenitor cell and cancer cell polarized motility and aligned morphology via a cytocompatible shape memory polymer scaffold. *Biomaterials* **140**, 150–161 (2017).
  27. Brasch, M. E. *et al.* Nuclear position relative to the Golgi body and nuclear orientation are differentially responsive indicators of cell polarized motility. *PLoS One* 1–19 (2019)  
doi:10.1371/journal.pone.0211408.
  28. Passucci, G., Brasch, M. E., Henderson, J. H., Zaburdaev, V. & Manning, M. L. Identifying the mechanism for superdiffusivity in mouse fibroblast motility. *PLoS Comput. Biol.* **15**, 1–16 (2019).
  29. Gong, T. *et al.* The Control of Mesenchymal Stem Cell Differentiation Using Dynamically Tunable Surface Microgrooves. *Adv. Healthc. Mater.* **3**, 1608–1619 (2014).

30. Luo, R., Wu, J., Dinh, N. D. & Chen, C. H. Gradient porous elastic hydrogels with shape-memory property and anisotropic responses for programmable locomotion. *Adv. Funct. Mater.* **25**, 7272–7279 (2015).
31. Gu, H., Lee, S. W., Buffington, S. L., Henderson, J. H. & Ren, D. On-Demand Removal of Bacterial Biofilms via Shape Memory Activation. *ACS Appl. Mater. Interfaces* 6–10 (2016) doi:10.1021/acsami.6b06900.
32. Wang, J. *et al.* Shape memory activation can affect cell seeding of shape memory polymer scaffolds designed for tissue engineering and regenerative medicine. *J. Mater. Sci. Mater. Med.* **28**, 1–9 (2017).
33. Zimkowski, M. M. *et al.* Integrating a novel shape memory polymer into surgical meshes decreases placement time in laparoscopic surgery: An in vitro and acute in vivo study. *J. Biomed. Mater. Res. - Part A* **101 A**, 2613–2620 (2013).
34. Zarek, M., Mansour, N., Shapira, S. & Cohn, D. 4D Printing of Shape Memory-Based Personalized Endoluminal Medical Devices. *Macromol. Rapid Commun.* **38**, 1–6 (2017).
35. Ligon, S. C., Liska, R., Stampfl, J., Gurr, M. & Mülhaupt, R. Polymers for 3D Printing and Customized Additive Manufacturing. *Chem. Rev.* **117**, 10212–10290 (2017).
36. Ge, Q. *et al.* Multimaterial 4D Printing with Tailorable Shape Memory Polymers. *Sci. Rep.* **6**, 1–12 (2016).
37. Ding, Z. *et al.* Direct 4D printing via active composite materials. *Sci. Adv.* **3**, (2017).
38. Jia, H., Gu, S. Y. & Chang, K. 3D printed self-expandable vascular stents from biodegradable shape memory polymer. *Adv. Polym. Technol.* **37**, 3222–3228 (2018).
39. Rychter, P. *et al.* Scaffolds with shape memory behavior for the treatment of large bone defects. *J. Biomed. Mater. Res. - Part A* **103**, 3503–3515 (2015).

40. Hu, G. F., Damanpack, A. R., Bodaghi, M. & Liao, W. H. Increasing dimension of structures by 4D printing shape memory polymers via fused deposition modeling. *Smart Mater. Struct.* **26**, (2017).

## Chapter 4: Programming via Printing

### 4.1 Introduction

Despite the demonstrated potential of SMPs across diverse fields, programming limitations have challenged wide-spread implementation of 4D printing. Traditionally, programming an SMP object, 3D printed or otherwise, is a separate and manual step, which requires a physical deformation of the SMP object<sup>1,2</sup>. Current programming techniques (e.g., stretching or compressing) only produce simple, often uniaxial, strains in the object, which limit shape changing to expansion, shrinkage, folding or twisting. More impactful and complicated part functions and geometries could require a more complex strain pattern within the object, such as localized strains or strain gradients, but are near impossible to manually create, especially in small and/or intricate geometries.

A means by which this limitation could potentially be overcome has been suggested in recent reports, which demonstrate induced strains during printing<sup>3-5</sup>. A localized stretching programming step is mimicked when the material is heated and extruded out of the nozzle, strain is induced in the material as it is pulled and cooled, similar to what we have observed in SMP electrospinning<sup>6-8</sup>. While trapped strains are often seen as a flaw in the 3D printing process due to potential warped or contracted final objects, the application of the strain trapping mechanism during printing to create devices that can change shape directly after printing has been largely unexplored. Achievement of self-morphing, 3D devices could lead to a fully automated fabrication process for 4D printed parts<sup>9,10</sup>. However, before that potentially transformative breakthrough can be realized, fundamental understanding of the extent to which strain can be trapped during the printing process must be achieved.

The goal of this study was to evaluate the extent to which strains can be intentionally trapped in the fibers during printing to achieve shape change without a manual programming step. To achieve this, SMP single line (1D) and single layer rectangular (2D) samples were printed while systematically varying temperature, extrusion speed, and fiber orientation. Samples were measured before and after recovery to calculate strain, and changes in shape (i.e., 1D to 2D, 2D to 3D) were observed. Later in this chapter (section 4.5), we demonstrate a proof of concept in 3D, multi-layer cubic (3D) samples were printed using the findings from 1D and 2D samples. The recovery behavior of the printed objects were also modeled with the long term goal of predicting shape change when using programming via printing (PvP).

## **4.2 Methods**

### **4.2.1 Experimental Design**

To determine the amount of strain that could be trapped into a single fiber, single 1D lines were printed at a constant speed with systematically varied temperatures and multipliers in order to evaluate factors that contribute to trapped strain. Additionally, single layer 2D rectangles were printed using the same temperatures and multipliers as the single line geometries and additionally printed with varied fiber orientations to determine the amount of trapped strain that could be programmed into a single layer of fibers and identify the resulting geometries once recovered. 2D samples were recovered uniaxially and freely to determine the linear strain and the strain in the fiber and the final geometry.

Lastly, 3D samples were printed using the results from the 1D and 2D samples to demonstrate a new programming approach, during fabrication, for ready-to-trigger SMP objects to use *in vitro* (see 4.5). Several 3D geometries were designed in CAD and printed: a cube that keeps a porous gradient upon recovery; prototype cell scaffolds using grid and hexagonal infill

patterns and a log pile to create pores that contract upon recovery; and finally, a hinge that bends upon recovery.

## **4.2.2 Materials**

The shape-memory thermoplastic polyurethane filament (MM4520 described in chapter 2) with a  $T_g$  of 45°C was printed using a modified (*see Chapter 2*) Makerbot Replicator 2X.

## **4.2.3 Sample Preparation**

### *4.2.3.1 Single Line Samples (1D)*

To trap strain into 1D fibers during printing, single lines (12 mm x 0.3 mm x 0.2 mm) were printed at a constant speed of 4200 mm/min using temperatures of 215°C and 225°C and an extrusion multiplier of 0.95 and 1.00. Five samples of each temperature and multiplier combination were printed. The build plate remained unheated for all printing in this chapter.

### *4.2.3.2 Single Layer Rectangular Samples (2D)*

Single-layer rectangular samples (28 mm x 8 mm x 0.2 mm) were printed at 4200 mm/min with the same temperatures and multipliers as the single line samples (4.2.3.1). Additionally, we varied the fiber orientation of each sample to 0°, 45°, or 90° (hereafter referred to as 0°, 45°, or 90° samples) with respect to the long axis. Eight samples of each set of parameters were printed.

## **4.2.4 Recovery and Strain Characterization**

### *4.2.4.1 Single Line Samples (1D)*

Samples were imaged and measured using a Hirox Digital Microscope (Model KH-8700). The linear measurement tool was used to measure the length of the original geometry. Samples were then recovered in a water bath at 70°C for 5 minutes. After recovery, the samples were re-measured. Programmed strain in each geometry was calculated by using the following equation:

$$\varepsilon = \frac{l_i - l_0}{l_0},$$

where  $l_0$  is the length before recovery and  $l_i$  is the length after recovery.

#### 4.2.4.2 Single Layer Rectangular Samples (2D)

Five samples of each experimental group were recovered using the DMA to determine uniaxial strain. Samples were fastened to the tension clamp and the temperature was ramped to 70°C at 5°C/min and held isothermally for 5 minutes, then ramped down 5°C/min to 25°C. Initial and recovered lengths were recorded and the strain was calculated using the equation above (4.2.4.1). The remaining three samples in each group were recovered freely in the water bath at 70°C to observe the final geometries.

#### 4.2.5 Modeling

To model the shape change due to the strains trapped within the object, a simple, hyper-elastic model adopted by decomposing the deformation gradient tensor  $\mathbf{F}$  into elastic and active components, which are characterized by  $\mathbf{F}^e$  and  $\mathbf{F}^p$ , respectively, such that

$$\mathbf{F} = \mathbf{F}^e \mathbf{F}^p, \quad (1)$$

where  $F_{ij} = \frac{\partial x_i}{\partial X_j}$ ,  $i, j = 1, 2, 3$ , and  $\mathbf{X}$  and  $\mathbf{x}$  are the configurations before and after deformation, respectively.

From our experiments, we observed contraction in the fiber direction ( $\mathbf{n}_p$ ), with little change along its orthogonal direction ( $\mathbf{m}_p$ ), and expansion in the normal direction  $\mathbf{e}_z$  due to the Poisson effect. From this, the active component  $\mathbf{F}^p$  was chosen as

$$\mathbf{F}^p = (1 - \epsilon_p) \mathbf{n}_p \otimes \mathbf{n}_p + \mathbf{m}_p \otimes \mathbf{m}_p + \frac{1}{(1 - \epsilon_p)} \mathbf{e}_z \otimes \mathbf{e}_z, \quad (2)$$

where,  $\mathbf{n}_p$  is the printing direction,  $\mathbf{m}_p$  is the orthogonal direction of  $\mathbf{n}_p$  on the printing plane,  $\mathbf{e}_z$  is the normal direction of the printing plane, and  $\epsilon_p$  is the residual strain. Furthermore, the strain energy density was expressed in terms of the elastic component  $\mathbf{F}^e$

$$U = \frac{1}{2}\mu(I_1^e - 3 - 2\ln J) + \frac{\lambda}{2}(\ln J)^2, \quad (3)$$

where  $\mu$  is the shear modulus,  $\lambda$  is the Lamé constant,  $I_1^e = \text{tr}(\mathbf{F}^{eT}\mathbf{F}^e)$  is the first invariant of the right Cauchy-Green deformation tensor associated with  $\mathbf{F}^e$  and  $J = \det(\mathbf{F}) = \det(\mathbf{F}^e)$  by noticing  $\det(\mathbf{F}^p) = 1$ . The shape changes were simulated using finite element analysis with implementation of the material model in the package FEniCS.

### 3.2.6 Statistical Analysis

Data from the 1D lines and 2D rectangular samples were evaluated using 2-way ANOVA, followed by Tukey post-hoc. Bars show sample standard deviation, and means were considered statistically different at  $p < 0.05$ .

## 4.3 Results

### 4.3.1 Single Line Samples (1D)

The single line samples curled upon recovery and transitioned from the original straight line into arcs and circles. Temperature had a significant effect on trapped strain ( $p = 0.02$ ) however, multiplier did not ( $p = 0.94$ ). Samples printed at a lower temperature trapped a higher mean strain ( $7.3 \pm 3.1\%$ ) compared to those printed a higher temperature ( $4.9 \pm 2.4\%$ ) (Figure 4-1, 4-2).

### 4.3.2 Single Layer Rectangular Samples (2D)

The  $0^\circ$  rectangular samples transitioned upon recovery from the original flat geometry into tubes along the short axis. The trapped strain in the rectangles was significantly affected by temperature ( $p = 0.0088$ ), with the lower temperature yielding higher mean strain ( $27.5 \pm 8.7\%$ )

compared to the higher temperature ( $16.3 \pm 7.8\%$ ) (Figure 4-3, 4-4). Neither multiplier, nor any interactions between temperature and multiplier were found to be significant.

The  $45^\circ$  rectangular samples also curled upon free recovery along the diagonal of the rectangle, specifically, along the fiber direction. Temperature had a significant effect on strain ( $p = 0.022$ ) with the lower temperature producing higher mean strain ( $14.7 \pm 8.3\%$ ) than the higher temperature ( $6.3 \pm 4.4\%$ ). Multiplier and interactions did not have a significant effect.

The  $90^\circ$  rectangular samples curled into tubes along the long axis in the direction of the fibers. Neither temperature nor multiplier had a significant effect on the amount of strain trapped in the long axis, and mean strains of all experimental groups withing this fiber orientation were approximately zero percent.

### **4.3.3 Models**

The simulation successfully captured the bending of the single line geometry, which is consistent with what was observed in our experiments. The bending is likely due to a non-uniform relaxation during printing, which upon cooling causes a gradient of trapped strain. As such, linearly distrusted residual strain field along the z-direction was adopted, (Figure 4-5) and an example of a printed single line was simulated with length (L) as 12 mm, thickness (t) as 0.3 mm, and width (w) as 0.3. The residual strain was set to 0.15 at the bottom surface ( $z=0$ ) and 0.03 at top surface ( $z=t$ ). The 2D rectangle was simulated with length (L) as 28 mm, width (w) as 8 mm, and thickness (t) as 0.2 mm. The printing direction is set up  $135^\circ$  (Figure 4-6A). As the value of residual strain was increased, the rectangle wrapped into a helix (Figure 4-6B).

## **4.4 Discussion**

We aimed to evaluate an approach to program SMP fibers during the printing process through systematic varying of printing parameters. Temperature was found to affect the strain

programmed in both 1D and 2D geometries. This could be explained by the fibers being drawn out of the nozzle, as the nozzle moves and the SMP cools, making it stretch. The cooler temperature creates a more viscous fiber, which then is pulled more, and creates more strain, than at higher temperatures with less viscous fibers.

Uniaxially-measured strain in the 2D samples were dependent on fiber orientation, likely due to anisotropy within the printed samples. All 2D rectangular samples were clamped into the DMA so that recovery was through the long axis of the sample. The fibers in the  $0^\circ$  samples were directly aligned with the recovery direction and, when the sample recovered, the entire contraction was measured. The fibers in the  $45^\circ$  samples were offset from the recovery direction by  $45^\circ$  and therefore the full fiber contraction was not entirely reflected in the recovery of the sample, showing a smaller amount of trapped strain in the sample for the same recovery direction. The samples printed at  $90^\circ$  were not affected by temperature or multiplier, likely because the programming direction was orthogonal to the recovery measuring direction. The averages were very close to  $0^\circ$ , and samples of both temperature and multiplier groups exhibited some negative strains. This is potentially the result of a small Poisson effect, where, as the fibers contract in length they expand in diameter and cause small increase in the length of the rectangle. Alternatively, it could be a result of anisotropic mechanical properties, where the material stretched due to the weight of the DMA clamp.

Fiber bending was present in recovered geometries of both 1D and 2D samples. This bending could potentially be explained by the cooling of the single layer, where the midline of the bottom portion (closest to the build plate) of the fiber cools more slowly due to the distance from the air. The material in all other outer surfaces of the fiber allow for faster cooling. Similar bending was found in 3D samples and was explained to be due to different trapped strain values

due to the different conditions that exist at each layer during the printing process<sup>3,4</sup>. For example, lower and middle layers are reheated as the nozzle deposits more molten polymer on top of them. Layers at the top do not get additional heat. Bodaghi et al. takes advantage of this process and has used this heating gradient model to predict the final geometry of solid 4D printed parts using input parameters of temperature and printing speed<sup>11</sup>.

The results from these experiments indicate that large strains can be programmed into 4D printed SMP objects when using a low printing temperature. This work also suggests that the greatest contraction of a 3D object will likely be in the direction of the printed fibers. Based on these outcomes, we performed a proof of concept study to demonstrate how PvP behaves in 3D, and how it could be implemented in biomedical applications.

## **4.5 Ready-to-Trigger 4D printed SMPs using PvP**

### **4.5.1 Sample Preparation**

Based on our findings from the previous experiments, all subsequent 3D samples were printed at 215°C with a multiplier of 1.0 and with the same speed and build plate settings as before.

#### *4.5.1.1 Porous Gradient Cube*

A 16 x 15 x 16 mm cube with pores of three different sizes (0.9 mm<sup>2</sup>, 6.5 mm<sup>2</sup>, and 0.48 mm<sup>2</sup>) was printed to observe changes in pore size and gradient (Figure 4-7). The fiber orientation was held constant in each layer, so that contraction would occur in only one direction.

#### *4.5.1.2 Porous Cell Scaffolds*

To print a porous cell scaffold, cubes measuring 9.5 x 9.5 x 9.5 mm were printed at 65% infill with a fiber orientation alternating between 0° and 90° per layer (Figure 4-8A). A

hexagonal infill was also used in some scaffolds to determine if a different contraction would occur (Figure 4-8B).

Additionally, an alternative porous scaffold was produced by printing a log pile, where each log (of the pile) was printed as a solid beam with a lengthwise uniform fiber orientation (Figure 4-9). Logs were rotated between 0° and 90° per layer to make a 7.5 x 7.0 x 4.6 mm porous cube.

#### 4.5.1.3 Hinge

Lastly a porous hinge was printed using 50% infill with alternating 0° and 90° fiber orientation per layer to demonstrate a bending effect. The hinge consisted of two 5 x 5 x 2.5 mm towers connected by a 3 x 5 x 1 mm rectangle at their base (Figure 4-10).

### 4.5.2 Characterization

#### 4.5.2.1 Porous cubes and scaffolds

The post-printed cube dimensions and pores were measured with the Hirox microscope, then recovered in the water bath at 70°C for 10 min. The dimensions and pores were remeasured, and the change in area was calculated using the following equation:

$$\varepsilon_A = \frac{A_0 - A_i}{A_0},$$

where  $A_0$  is the area before recovery and  $A_i$  is the area after recovery. The pores sizes of the hexagonally infilled scaffolds were measured using ImageJ.

### 4.5.4 Results

#### 4.5.4.1 Porous Gradient Cube

The cube contracted in the direction of printing and the dimensions changed from 16 x 15 x 16 mm to 16 x 12 x 18 mm. The total area of the top of the cube changed by 20%. Large pores contracted to  $33.0 \pm 2.9\%$  of their original area, while the medium and small pores contracted

55.3 ± 18.3% and 51.9 ± 8.2%, respectively. The pore gradient remained intact even after contraction.

#### 4.5.4.2 Porous Cube Scaffolds

The scaffold cube with fiber orientation alternating between 0° and 90° contracted in both fiber directions for a 35.4% change in area (change in L x W was 1.48 mm x 1.86 mm) and the area of the pores decreased 49.9 ± 3.2%. The scaffold cube with hexagon fiber orientation contracted in both fiber directions for a 34.8% change in area (change in L x W was 1.95 mm x 1.89 mm) while the area of the pores decreased 80.6 ± 6.3%.

#### 4.5.4.3 Log Pile

The scaffold cube with fiber orientation alternating between 0° and 90° contracted in both fiber directions for a 25.9% change in area (change in L x W was 0.93 mm x 0.71 mm) and the area of the pores decreased 74.6 ± 7.3%.

#### 4.5.4.4 Hinge

The hinge bent from the center of the hinge through its length to a 120° angle. No secondary bending in the orthogonal direction was present.

#### 4.5.4.5 Modeling

A cube with a porous lattice was simulated where fiber orientation was in a uniform direction (along x-axis) (Figure 4-11). Upon triggering there is contraction in the x direction and expansion in the z direction, while the y direction remains unchanged, which was what we observed in our porous gradient cube geometry.

### 4.5.5 Discussion

While Bodaghi et al. suggested a potentially promising way to produce ready-to-trigger SMP parts, it did not account for porous structures, which are desirable in biomedical

applications for roles such as cell and tissue scaffolds or wound and defect filling constructs. All of our 3D samples exhibited strain release upon recovery, even with the addition of pores and fibers stretching across gaps. The porous cube with three different pore sizes yielded a geometry with its pore sized reduced up to 55% with the pore gradient still intact post recovery.

The porous cube scaffolds demonstrated that strains could be programed in single fibers that reach across gaps. We saw a 35.4% change in area, however the contractions in the 0° and 90° directions were not uniform. This suggests that the fusion points where each fiber connects to its orthogonal neighbor acts as an anchor and impedes the strain release, potentially due to a 2D Poisson effect. This prompted us to print an auxetic cube, that is, a structure with a negative Poisson's ratio. The cube with the hexagon infill had a similar total areal contraction, however, contractions in the 0° and 90° direction were much more uniform and amount of contraction of the pores increased greatly. This could have implications in tissue engineering applications to create small pore sizes that are physiologically relevant to cells considering the inadequate resolution of many off-the-shelf printers.

The log pile showed how beams or “logs” of solid material would behave over gaps. As described above, Bodaghi showed a bending phenomenon as trapped strains are released from solid 4D printed SMPs<sup>3</sup>. Here, we did not see bending logs, likely due to the multiple contact points of orthogonal logs. However, the pores in the log pile contracted 74%, which was about 25% larger than what was observed in the scaffold cube. This could be due to the combined contraction of the log lengths and increase in log width due to the Poisson effect.

The hinge bent the opposite direction of the 2D samples, that is, it bent down towards the first layer, rather than up towards the top layer. We speculate that this largely due to the geometry. Unlike the 2D rectangles, the base of the hinge is porous (i.e., individual fibers in

contact with the build plate) which could contribute to more rapid cooling, similar to the single line bending, which also curled downwards. We also did not observe any secondary bending along the short axis, which could be attributed to additional material at the ends of the hinge (i.e., the tower height) act as a passive constraint that prevents bending.

## **4.6 Conclusions**

This work demonstrated a critical first step in achieving self-morphing SMP parts. We successfully quantified and modeled the strains trapped in 1D, 2D, and 3D SMP objects during the printing process. From these experiments, it was revealed that the shape change of the recovered geometries is due to contraction of the fibers, and therefore the largest strains were observed in the direction of the fiber orientation. In chapter 5, we used our findings from these experiments to show how PVP could be advantageous in a biomedical application.

*Additional acknowledgements for this chapter:* Prof. Teng Zhang and his students, Di Liu and Hongyu Fan, for their modeling and simulation work; Paul Chando and Dr. Pranav Soman for their expertise in 3D printing fabrication, and Chi Chi Tong for his assistance with CAD and printing preparation.

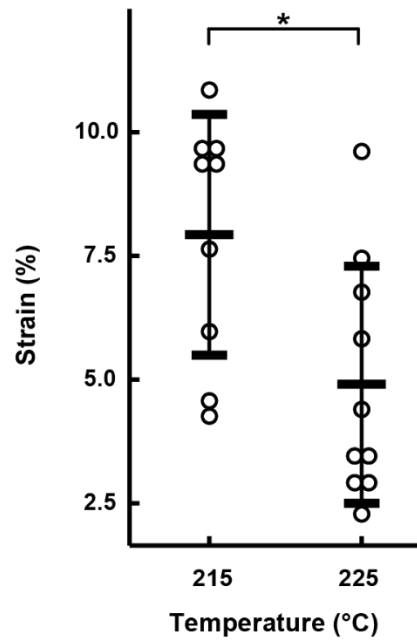


**Figure 4-1.** Temperature affects trapped strain in single line samples. Lower printing temperature led to an increase in mean trapped strain. (\*  $p < 0.05$ ; two-way ANOVA).

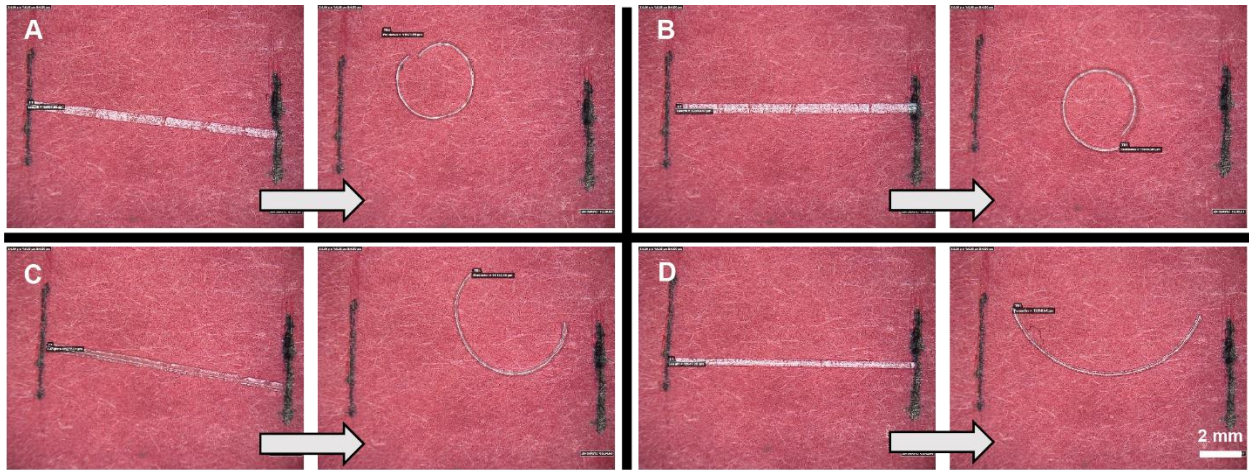


**Figure 4-2.** Representative images of the single line geometry before and after recovery when printed at temperatures of 215°C (A, C) or 225°C (B, D) with an extrusion multiplier of 1.0 (A, B) or 0.95 (C, D).

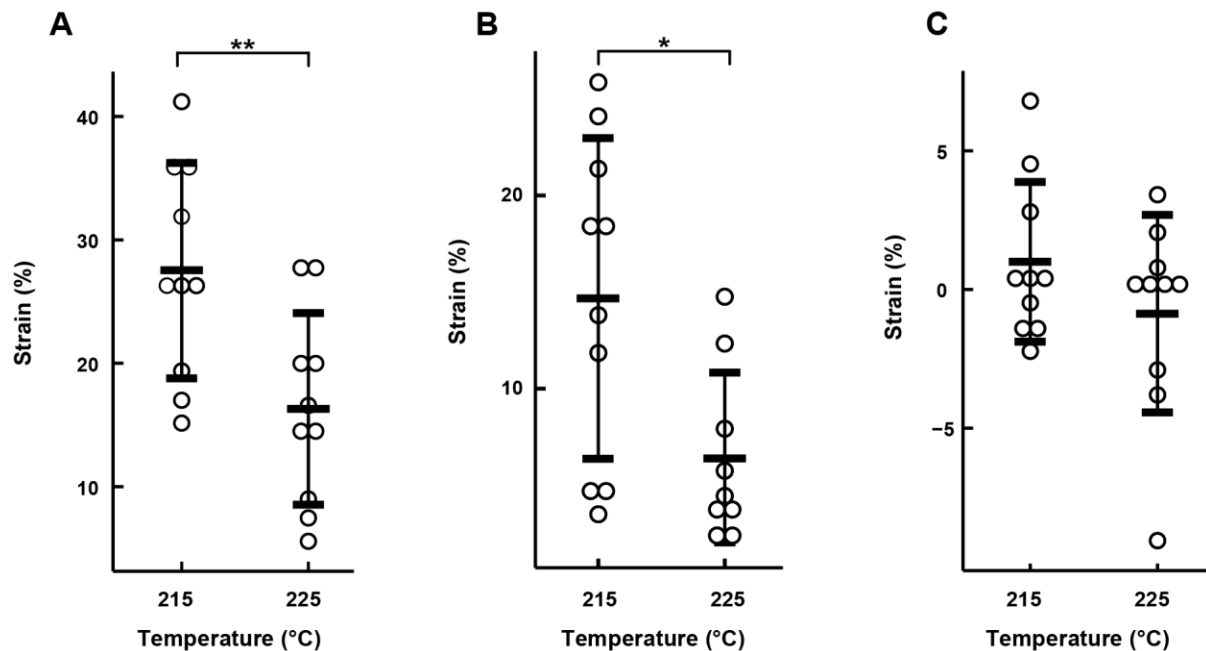


**Figure 4-3.** Printing temperature affects trapped strain in 2D samples with fiber orientations of 0° (A) and 45° (B) when measured along the long axis. Temperature had no significant impact on the strain in the 90° orientation (C). (\*  $p < 0.05$ ; \*\*  $p < 0.01$ , two-way ANOVA). Note: scales on the Strain (%) axis change.

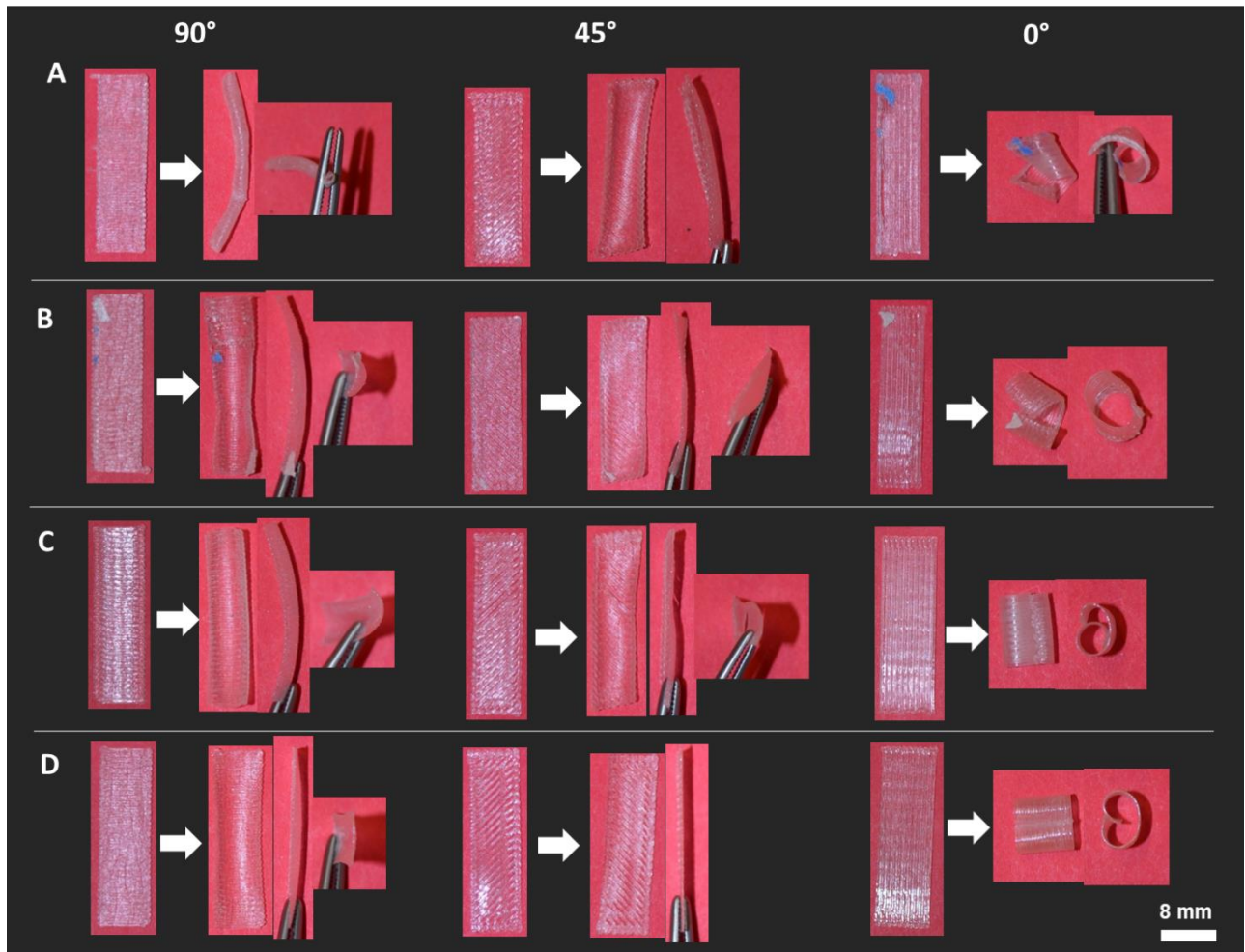


**Figure 4-4.** Representative images of the free recovery behavior in 2D rectangular samples printed with varied printing parameters (printing temperature/multiplier) by row: (A) 215°C/1.0, (B) 225°C/1.0, (C) 215°C/0.95, (D) 225°C/0.95. In addition to bending in the long axis, a secondary bend can be seen along the short axis, particularly in the 90° samples.

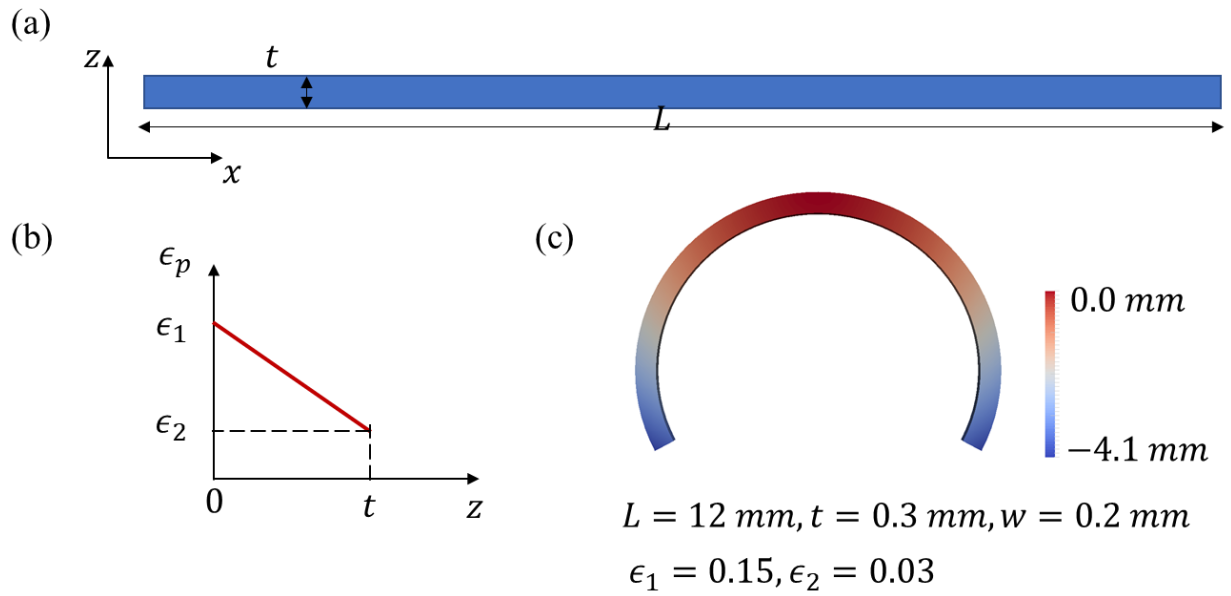


**Figure 4-5.** (a) The schematic of a 1D printed fiber. (b) Gradient of the residual strain along the  $z$ -direction (normal to the printing plane). (c) A representative example of curved fiber after triggering ( $w$  is the width of the fiber). The color indicates the displacement of  $z$ -direction.

*Figure provided by Zhang Lab.*

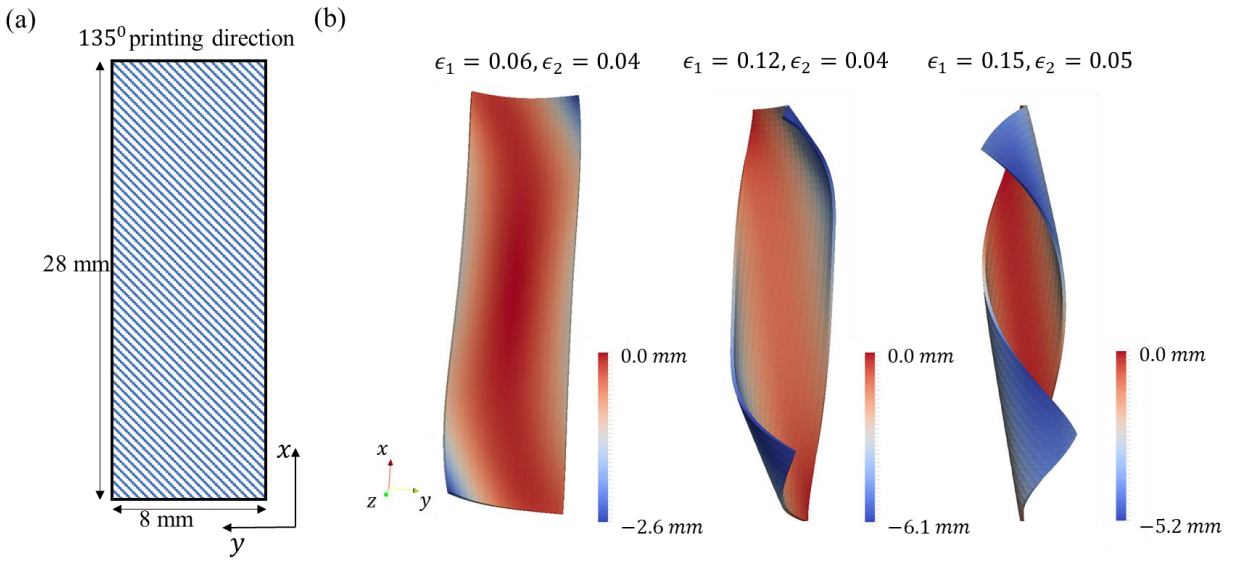


**Figure 4-6.** (a) The schematic of a 2D printed plate with the fiber orientation as 45 degrees and thickness ( $t$ ) as 0.2 mm. (b) Deformed configurations of the plate at different levels of the residual strain. The color indicates the displacement of  $z$ -direction. *Figure provided by Zhang Lab.*

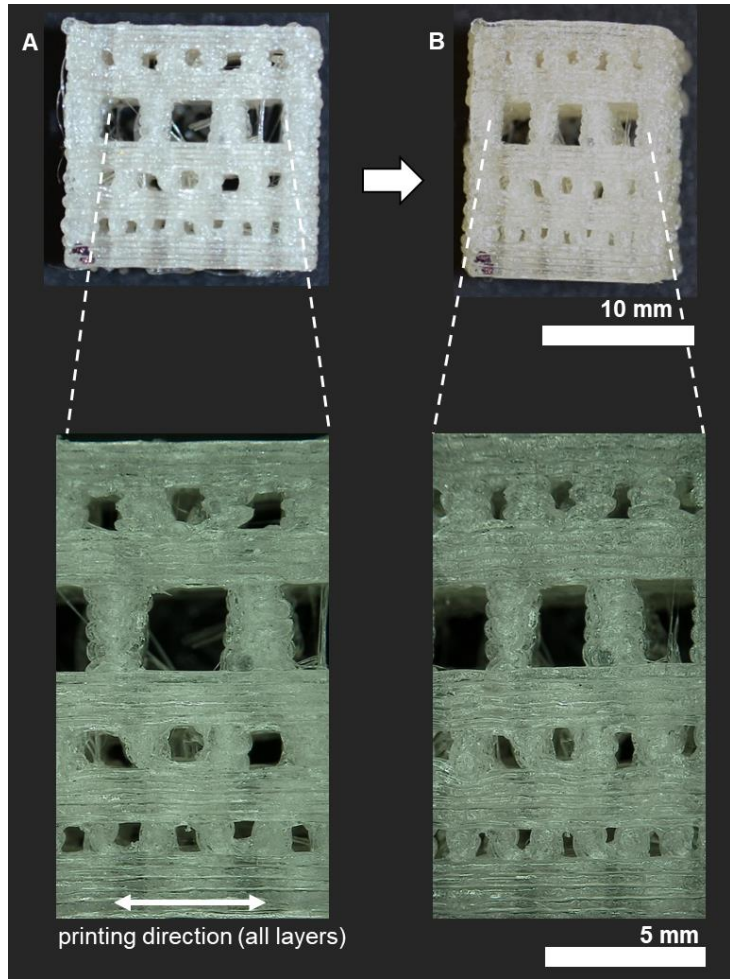


**Figure 4-7.** Representative image of the cube with three different pore sizes (small, medium, large, from bottom). All pores contracted in the direction of the fibers and the pore gradient was conserved.

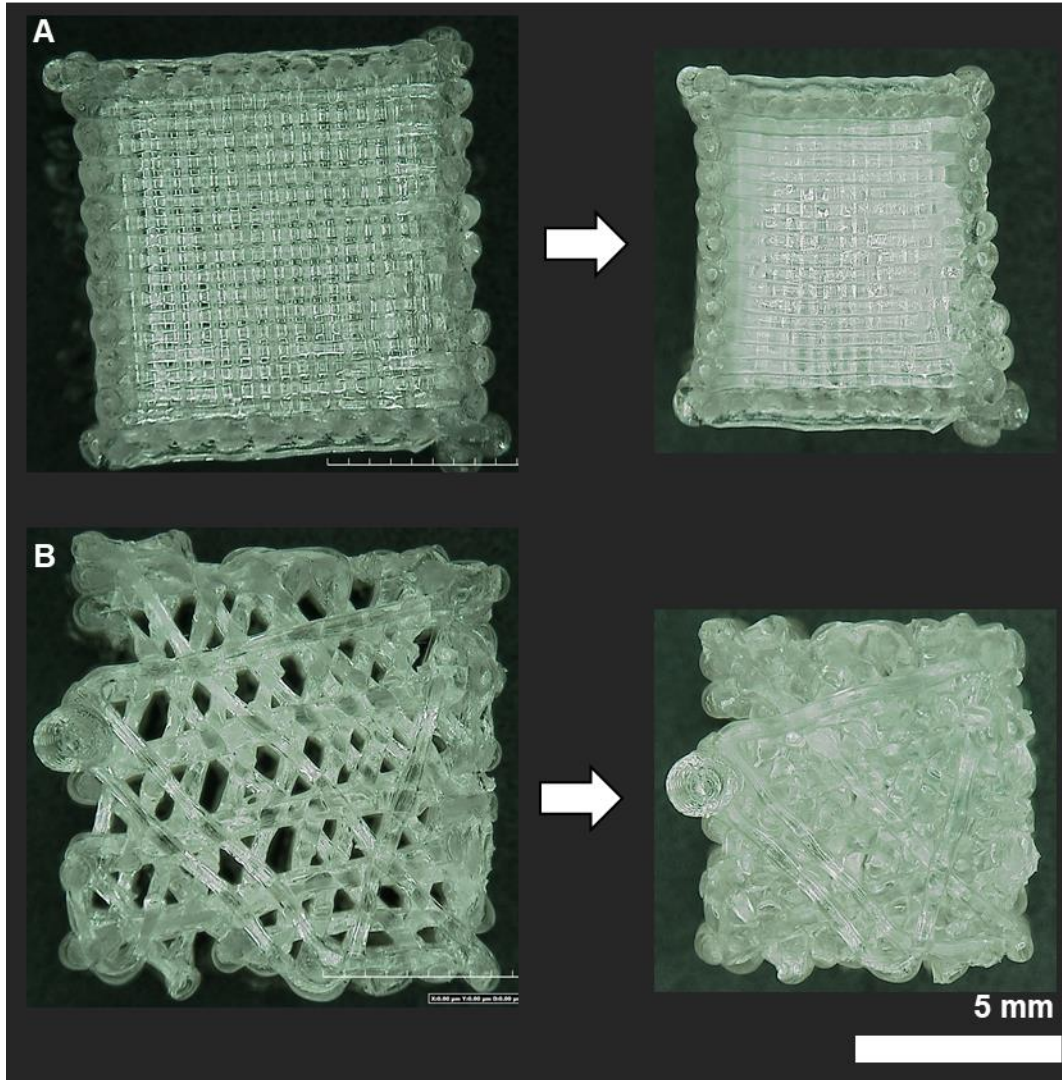


**Figure 4-8.** Representative image of cubes printed for cell scaffolding with (A) alternating 0° and 90°, and (B) hexagonal infill. The hexagonal infill led to a more uniform contraction upon recovery.

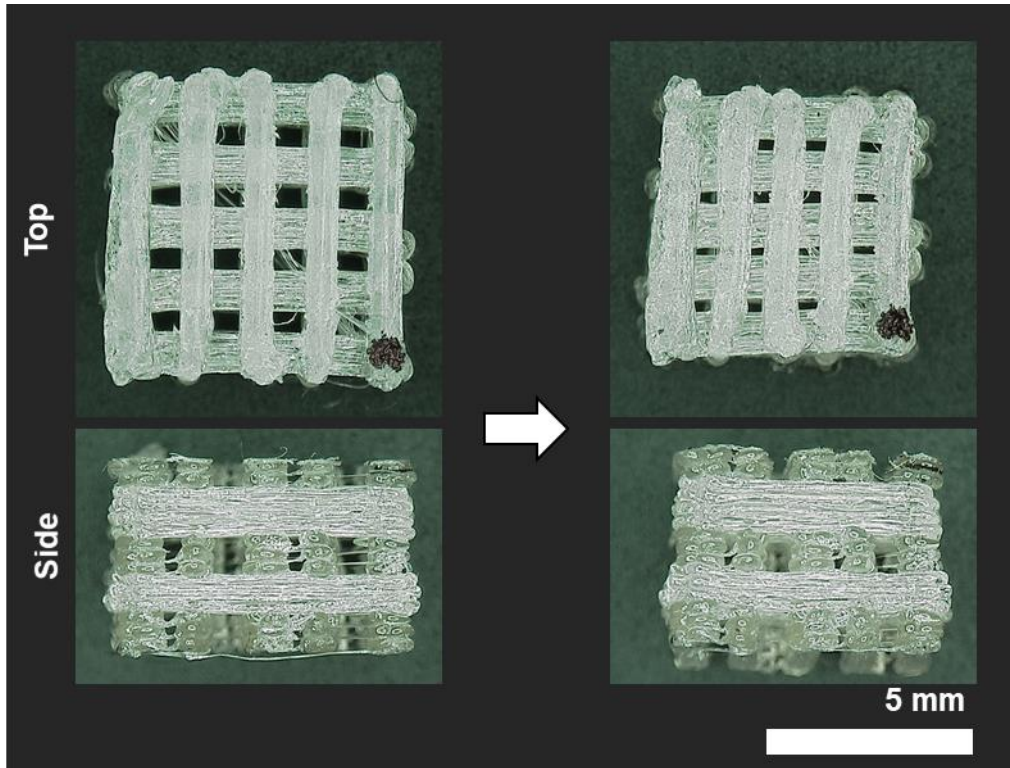


**Figure 4-9.** Representative image of top and side views of the log pile cell scaffold. Pore size decreased dramatically after recovery, and a Poisson effect is seen in the side view.

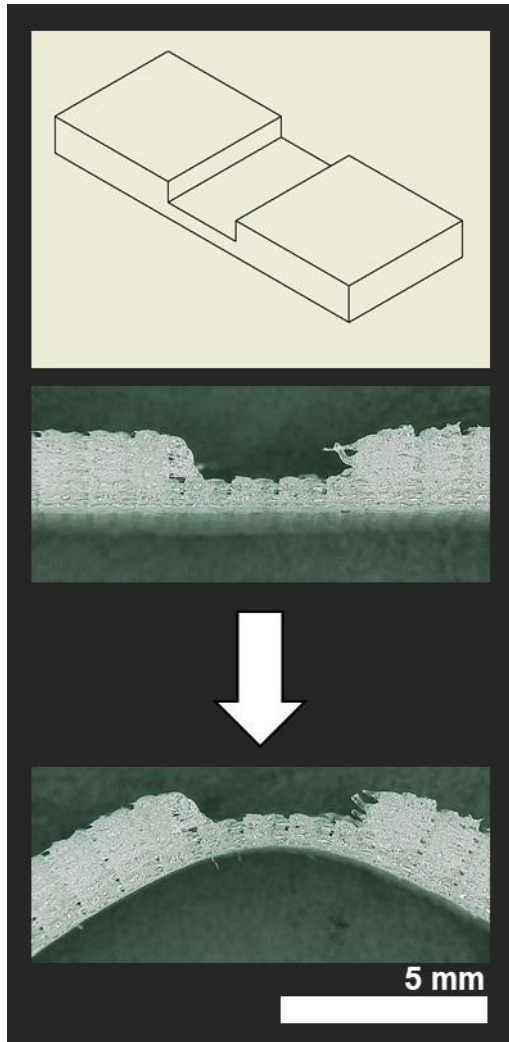


**Figure 4-10.** Representative image of the porous hinge. Top panel shows a CAD drawing of the hinge geometry. A large, downward, bending can be seen after recovery.

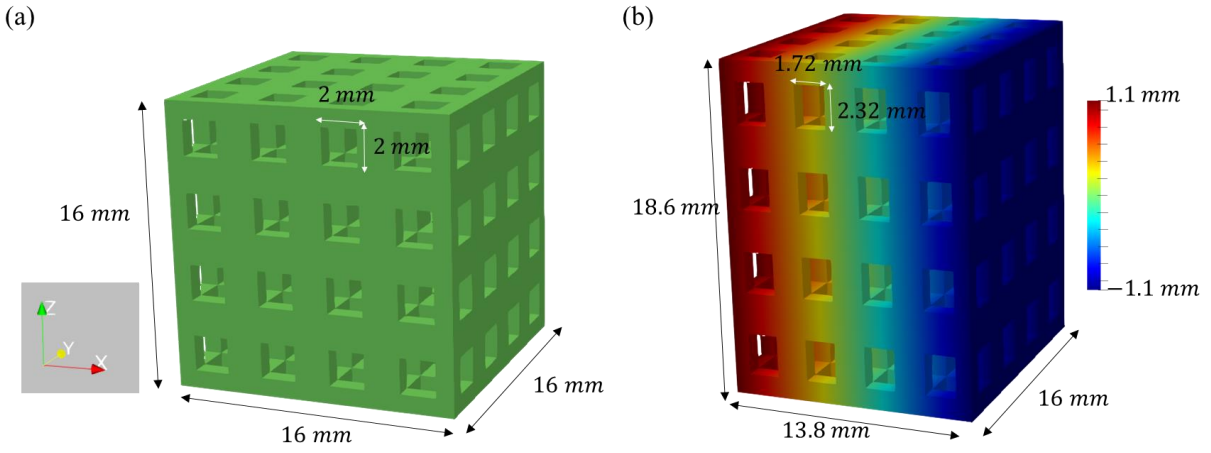


**Figure 4-11.** (a) The initial structure of a cube lattice. (b) Deformed configurations of the cube.

The color indicates the displacement of x-direction. *Figure provided by Zhang Lab.*

## 4.6 References

1. Mather, P. T., Luo, X. & Rousseau, I. A. Shape Memory Polymer Research. *Annu. Rev. Mater. Res.* **39**, 445–471 (2009).
2. Rousseau, I. A. Challenges of Shape Memory Polymers : A Review of the Progress Toward Overcoming SMP's Limitations. *Polymer Engineering and Science.* (2008) doi:10.1002/pen
3. Bodaghi, M., Damanpack, A. R. & Liao, W. H. Adaptive metamaterials by functionally graded 4D printing. *Mater. Des.* **135**, 26–36 (2017).
4. Hu, G. F., Damanpack, A. R., Bodaghi, M. & Liao, W. H. Increasing dimension of structures by 4D printing shape memory polymers via fused deposition modeling. *Smart Mater. Struct.* **26**, (2017).
5. Abuzaid, W., Alkhader, M. & Omari, M. Experimental analysis of heterogeneous shape recovery in 4d printed honeycomb structures. *Polym. Test.* **68**, 100–109 (2018).
6. Tseng, L. F., Mather, P. T. & Henderson, J. H. Shape-memory-actuated change in scaffold fiber alignment directs stem cell morphology. *Acta Biomater.* **9**, 8790–8801 (2013).
7. Baker, R. M., Tseng, L.-F., Iannolo, M. T., Oest, M. E. & Henderson, J. H. Self-deploying shape memory polymer scaffolds for grafting and stabilizing complex bone defects: A mouse femoral segmental defect study. *Biomaterials* **76**, 388–398 (2016).
8. Wang, J., Quach, A., Brasch, M. E., Turner, C. E. & Henderson, J. H. On-command on / off switching of progenitor cell and cancer cell polarized motility and aligned morphology via a cytocompatible shape memory polymer scaffold. *Biomaterials* **140**, 150–161 (2017).
9. Ge, Q. *et al.* Multimaterial 4D Printing with Tailorable Shape Memory Polymers. *Sci. Rep.* **6**, 1–12 (2016).

10. Mao, Y. *et al.* Sequential Self-Folding Structures by 3D Printed Digital Shape Memory Polymers. 1–12 doi:10.1038/srep13616.
11. Noroozi, R., Bodaghi, M., Jafari, H. & Zolfagharian, A. Shape-Adaptive Metastructures with Variable Bandgap Regions by 4D Printing. (2020).

## Chapter 5: Confirming Cytocompatibility and Utilizing PVP *in Vitro*

### 5.1 Introduction and Background

Prior reports on the cytocompatibility of shape memory polyurethanes and cell interaction both *in vivo* and *in vitro* have been well documented<sup>1,2</sup>. Fare et al studied human fibroblast cells lines and the cytotoxicity of SMP MM5520 ( $T_g = 55^\circ\text{C}$ ), a similar material from the same manufacturer as MM4520 ( $T_g = 45^\circ\text{C}$ )<sup>3</sup>. Another study by De Nardo studied both SMP MM5520 and SMP MM3520 ( $T_g$  of  $35^\circ\text{C}$ ) and reported low cytotoxicity and good cell colonization on both materials<sup>4</sup>. While both studies make a good case for cytocompatibility, the material substrates were not 3D printed. There are fewer reports on the cytocompatibility of SMP MM4520<sup>5</sup>. As few reports of 3D printed SMP MM4520 contain cytotoxicity assays, we were interested in the potential effects of printing parameters on cell viability, along with conducting our own confirmation of the low cytotoxicity of SMP MM4520.

Additionally, in this chapter, we demonstrate a potential *in vitro* application of programming via printing (PvP). 3D cell culture is used *in vitro* because it imitates *in vivo* environments and provides proper microenvironments and cell-cell interactions compared to 2D culture<sup>6-12</sup>. These characteristics make 3D culture a potentially powerful research tool, however, it is not without limitations. A known issue in developing robust tissues from 3D scaffolds is obtaining an even cell distribution<sup>6</sup>. Tissues grown from non-uniform and low cell densities are often inferior to their uniform/high cell density counterparts<sup>13</sup>. To remedy this, common practice is to use active cell seeding techniques, such as vacuum or spin seeding, however, such methods can potentially damage cells due to high shear stress, which can lead to a loss in viability<sup>14,15</sup>. In chapter 4 we observed large pore contractions in our 4D printed scaffold cubes. Here, we use this

understanding to print an open, porous, 3D scaffold passively seeded with cells, which is then contracted during culture to obtain smaller pores.

This chapter contains three studies using SMP MM4520 and cells to address the following objectives: first, to confirm the low cytotoxicity of SMP MM4520; second, to determine the extent to which the printing parameters utilized in chapter 3 affected cell viability; and third, to demonstrate a potential biomedical application for the PVP work in chapter 4.

## **5.2 Methods**

### **5.2.1 Cytocompatibility of SMP MM4520**

To confirm previous reported cytocompatibility of SMP MM4520, flat 9.0 x 9.0 x 0.4 mm samples were hot-pressed at 225°C or printed at 225°C. Control samples were cut from tissue culture polystyrene (TCPS) into 9 x 9 mm pieces. All SMP and control samples were sterilized in ethanol for 1 hour and dried for 24 hours, then rinsed in sterile PBS and conditioned with Basal Medium Eagle (BME) with 10% fetal bovine serum for 1 hour to help with cell attachment.

C3H10T1/2 murine fibroblasts (ATCC) were cultured in Basal Medium Eagle (BME) supplemented with 10% Fetal Bovine Serum (FBS), 1% GlutaMAX, and 1% Penicillin-Streptomycin (all purchased from Invitrogen). Cells were sub-cultured at 70% confluence following ATCC recommendations. Cells were collected and used for experiments at passage number fifteen. Cells were droplet seeded 15,000 cells/mL onto all samples and incubated at 37°C for 48 hours. Samples were then stained with LIVE/DEAD (Invitrogen) reagents, Calcein AM and Ethidium Homodimer, as per the manufacturer's instructions, and imaged at 10X through a Leica DMI 4000B inverted fluorescent microscope with a Leica DFC 340FX camera. Cells were counted manually, and viability was calculated by dividing the number of live cells

by the total number of cells. This method was repeated for the cytocompatibility study with varied printing parameters.

### **5.2.2 Cytocompatibility of 3D Printed SMP MM4520 Using Varied Parameters**

To determine the extent to which printing parameters affect cell viability on the 3D printed SMP, flat 9.0 x 9.0 x 0.4 mm samples were printed with the same systematically varied temperature (215°C or 225°C) and multiplier (0.95 or 1.0) while speed and infill were held constant at 3600 mm/min and 100%, respectively. Fiber orientation was not studied because it is a macroscopic, not microscopic, property and not expected to affect cell behavior. Control samples, cell culture and seeding, and viability assays were carried out as described in the previous section (*see 5.2.1*).

### **5.2.3 Distribution of Cells in SMP Scaffold Using Programming via Printing**

To demonstrate the impact of PvP in 3D cell culture, the distributions of fibroblasts through 3D printed SMP scaffolds were analyzed. Based on our findings in Chapter 4, that lower temperatures lead to increased strains and therefore higher contractions, a 9 x 9 x 8 mm scaffold was designed to be printed at 210°C with a multiplier of 1.0. Infill was set to 65% with a hexagonal pattern, which was rotated 90° each layer to create pores. The scaffolds were sterilized in ethanol and conditioned as described above (*see 5.2.2*). Scaffolds were divided into four groups: pre-triggered 40°C, active 40°C, pre-triggered 70°C, and active 70°C. Pre-triggered scaffolds were recovered in sterile PBS at 40°C or 70°C before conditioning and seeding.

Cells were droplet seeded onto the scaffolds at 30,000 cells/cm<sup>3</sup> and incubated at 30°C. After 2 hours, the active 40°C scaffolds were transferred to a 40°C incubator for 22 hours to fully recover. The active 70°C and both pre-triggered groups remained in the 30°C incubator for the entire 24 hours. Afterwards, cells were fixed to their scaffolds using 4% paraformaldehyde. The active 70°C were then recovered in 70°C PBS. Next, three scaffolds from each group were cut

with a razor blade from top to bottom through the center. Cells were treated with triton solution to permeate the cells, and DAPI stain (Invitrogen) was applied following the manufacturer's instructions.

Cells were imaged using the multi acquisition option in micromanager. The X-Y position was manually set in order to image the entire scaffold cross section and Z-stacks of images were taken at each position with nine 100 um increments for a total depth of field of 0.9 mm through the 5X lens. To create a single image with the entire depth of field, each z-stack was loaded into ImageJ and run through the "Extended Depth of Field" plugin<sup>16</sup>. To isolate the cells in the image, the threshold was manually adjusted and run through the "Watershed" function<sup>17</sup>. Then, to both count and record the positions the cells, the adjusted image was run through the "Analyze Particles" function<sup>17</sup>. The labeled Y positions of the cells were normalized with respect to the length of their scaffolds, and the number of cells in the top, middle, and bottom third was quantified.

## **5.2.4 Analysis and Statistics**

### *5.2.4.1 Cytocompatibility*

Comparisons between viability of cells on pressed, printed, and TCPS control samples were made via one-way ANOVA, while comparisons of viability on 3D printed samples with varied parameters were made using two-way ANOVA. Means were considered statistically different at  $p < 0.05$ .

### *5.2.4.2 Distribution*

Student's t-test was used to determine if the difference in cell number was significant in each third of the scaffold. A t-test was also used to determine if the total number of cells was significant. Results were considered significant at  $p < 0.05$ .

## 5.3 Results

### 5.3.1 Cytocompatibility of SMP MM4520

There was a significant difference between printed samples and the pressed and control samples ( $p = 0.008$  and  $p = 0.009$ , respectively) (Figure 5-1). No significant difference was detected between the pressed and control samples ( $p = 0.9$ ). The total cell numbers for all scaffold types were not significantly different ( $p = 0.4$ ). The hot-pressed MM4520 samples had a mean viability of  $97.8 \pm 0.75\%$  and a total cell count ranging from 129 to 340 cells/sample field of view with a mean total cell count of  $204 \pm 122$  cells/sample field of view. The printed MM4520 samples had a mean viability of  $94.7 \pm 0.99\%$  and a total cell count ranging from 120 to 271 cells/sample with a mean total cell count of  $206 \pm 55$  cells/sample field of view. The TCPS control samples had a mean viability of  $97.8 \pm 0.66\%$  and a total cell count ranging from 257 to 353 cells/sample field of view with a mean total cell count of  $296 \pm 60$  cells/sample field of view.

### 5.3.2 Cytocompatibility of 3D Printed SMP MM4520 Using Varied Parameters

Multiplier was found to significantly affect viability ( $p = 0.0003$ ). There was no significant difference detected for temperature ( $p = 0.46$ ) or interactions ( $p = 0.69$ ) (Figure 5-2). The total cell numbers for all samples were not significantly different ( $p > 0.05$ ). The cell viability of all samples was  $>90\%$  which suggests reasonable cytocompatibility. The samples printed at  $215^\circ\text{C}$  and a multiplier of 1.0 had a mean viability of  $93.2 \pm 0.89\%$  and a total cell count ranging from 107 to 558 cells/sample with a mean total cell count of  $270 \pm 150$  cells/sample field of view. The samples printed at  $215^\circ\text{C}$  and a multiplier of 0.95 had a mean viability of  $95.6 \pm 1.24\%$  and a total cell count ranging from 121 to 352 cells/sample field of view with a mean total cell count of  $212 \pm 121$  cells/sample field of view. The samples printed at  $225^\circ\text{C}$  and a multiplier of 1.0 had a mean viability of  $92.4 \pm 0.51\%$  and a total cell count ranging

from 209 to 314 cells/sample field of view with a mean total cell count of  $263 \pm 53$  cells/sample field of view. The samples printed at  $225^{\circ}\text{C}$  and a multiplier of 0.95 had a mean viability of  $96.3 \pm 0.42\%$  and a total cell count ranging from 151 to 240 cells/sample field of view with a mean total cell count of  $203 \pm 46$  cells/sample field of view.

### **5.3.3 Distribution of Cells in SMP Scaffold Using Programming via Printing**

#### *5.3.3.1 Active and Pre-triggered $40^{\circ}\text{C}$*

Scaffold pores contacted by a mean of  $32.3 \pm 4.1\%$  compared to the as-printed pore size. There was a significant difference between the PVP scaffolds and the pre-triggered scaffolds with the top third and bottom third ( $p = 0.012$  and  $p = 0.0006$ , respectively). No significant difference was found for the total number of cells in each scaffold. The active  $40^{\circ}\text{C}$  scaffolds contained a mean of  $33 \pm 3.6$  cells,  $32 \pm 4.0$  cells, and  $35 \pm 1.0$  cells in the top, middle, and bottom thirds of the scaffold (per depth of field), respectively (Figure 5-3A; Figure 5-4B). The total average cell count for the depth of field was  $135 \pm 18.0$  cells. The pre-triggered  $40^{\circ}\text{C}$  samples contained a mean of  $42 \pm 2.0$  cells,  $36 \pm 3.0$  cells, and  $22 \pm 2$  cells in the top, middle, and bottom thirds of the scaffold (per depth of field), respectively (Figure 5-4). The total average cell count for the depth of field was  $146 \pm 10.0$  cells (Figure 5-3B).

#### *5.3.3.2 Active and Pre-triggered $70^{\circ}\text{C}$*

Scaffold pores contacted by a mean of  $79.1 \pm 5.3\%$  compared to the as-printed pore size. There was a significant difference between the active and pre-triggered scaffolds within the top third and middle third ( $p = 0.0005$  and  $p = 0.00006$ , respectively) (Figure 5-3C; Figure 5-4D). There was also a significant difference detected between the total number of cells in each scaffold ( $p = 0.0004$ ). The active  $70^{\circ}\text{C}$  scaffolds contained a mean of  $29 \pm 2.0$  cells,  $40 \pm 2.0$  cells, and  $30 \pm 1.0$  cells in the top, middle, and bottom thirds of the scaffold (per depth of field),

respectively (Figure 5-4C). The total average cell count for the depth of field was  $164 \pm 5.0$  cells (Figure 5-3D). The pre-triggered 70°C scaffolds contained a mean of  $37 \pm 1.0$  cells,  $31 \pm 1.0$  cells, and  $32 \pm 2$  cells in the top, middle, and bottom thirds of the scaffold (per depth of field), respectively. The total mean cell count for the depth of field was  $102 \pm 8.0$  cells.

## **5.4 Discussion**

### **5.4.1 Cytocompatibility of SMP MM4520**

We confirmed compatibility of SMP MM4520 *in vitro*. The C3H10T1/2 cell line was chosen because of its previous use in the development and applications of cytocompatible SMPs<sup>18,19</sup>. The cell viability of SMP MM4520 under different fabrication methods was greater than 90% and considered to have good cytocompatibility. These numbers are similar to those reported by Fare et al, who, through use of a lactate dehydrogenase (LDH) assay, found that there were negligible levels of LDH activity from a period of 3h to 7 days of exposure to the MM5520 material, indicating very low cytotoxicity.

Low total cell numbers between MM4520 and the TCPS control is likely due to cell attachment. TCPS is treated to promote attachment, while the MM4520 samples were only conditioned with media, thus in the washing portions of the staining process, the cells became detached. Similar findings were reported by Fare, et al who ran adhesion tests on non-coated and protein coated (Fn, Fbg, CI, CII) disks of MM5520 and found that coating increased adhesion.

### **5.4.2 Cytocompatibility of 3D Printed SMP MM4520 Using Varied Parameters**

We also confirmed the cytocompatibility of the SMP under various printing conditions. Cell viability for all printed samples was above 90%, representative of a high degree of viability, which supports the low cytotoxicity findings from previous reports. A reduced multiplier contributed to a higher cell viability, which could potentially be explained by the resulting reduction in fiber diameter that could produce small spaces between the fibers and create a

suitable microenvironment that includes qualities such as proximity to other cells, minimal stress, increased adhesion, and maintenance of temperature and nutrients.

#### **5.4.3 Distribution of Cells in SMP Scaffold Using Programming via Printing**

In this work, a preliminary investigation of the application of PvP *in vitro* was conducted. Distribution was quantified by counting the number of cells in each third of the scaffold. The number of cells in the top third portions of the active 40°C scaffolds were significantly different from that of the pre-triggered 40°C. This suggests that the active scaffolds, which had a larger pore size upon cell seeding, allowed the cells to travel through the scaffold with less difficulty, than the smaller pores of the pre-triggered scaffold. A reduction in area led to some pores becoming very narrow, which could also inhibit cell travel. This could also explain the significant increase in cells in the bottom third of the active scaffold compared to the pre-triggered, as more cells could easily navigate through to reach the bottom.

Similar to the 40°C groups, the scaffolds contracted at 70°C showed a significant difference in cell percentage in the top third of the scaffold. Again, this is likely attributed to the ability of the cells to travel through the PvP scaffold. The total number of cells present in the PvP scaffold was significantly greater than that of the pre-triggered. In the 70°C scaffolds, the average decrease in pore size was 75%. This could account for the difference in cell numbers because when the cells were seeded on to the pre-triggered scaffold, the cells were not able to travel through the smaller pores as easily as the PvP scaffold, and many may have remained on the scaffold surface.

We chose to study active and pre-triggered scaffolds at 70°C because a greater contraction is obtained at higher temperature<sup>20</sup>. This is likely due to rapid heating of the structure which allows the fibers in the scaffold to contract in unison. Conversely, the increase in temperature from 30°C to 40°C may not have been powerful enough to transition the entire

scaffold to its rubbery phase, resulting in partial strain release. This shows how PvP could be advantageous, especially with very small pores. To obtain a similar effect during cell culture, a SMP with a lower  $T_g$  could be used.

This work offers a demonstration of PvP to obtain increased cell distribution within a 3D scaffold and has implications *in vitro*, where getting an even distribution of cells through a 3D scaffold is difficult without additional techniques such as vacuum seeding. PvP could be a valuable tool in tissue engineering and regenerative medicine, where scaffolds of high cell density and uniform distribution are needed to produce tissues, whereas lower densities and non-uniform cells contribute to substandard tissues<sup>21</sup>.

## 5.5 Conclusion

Through the experiments conducted in this chapter, we confirmed cytocompatibility of SMP MM4520 across different modes of substrate preparation. Among the 3D printed samples, we showed that a lower extrusion multiplier lead to an increased cell viability. Additionally, we were able to successfully demonstrate the use of a PvP scaffold to increase the percentage of cells that travel through a 3D scaffold. This helps confirm potential for using PvP to optimize cell seeding of *in vitro* 3D scaffolds to produce uniform tissues. Together, the studies in this chapter support the use of 3D printing SMP MM4520 in biomedical applications.

*Additional acknowledgements for this chapter:* Tackla Winston and Plansky Hoang for assisting with troubleshooting, and Shelby Buffington and Michelle Pede for general guidance with, and training for cell culture assays.

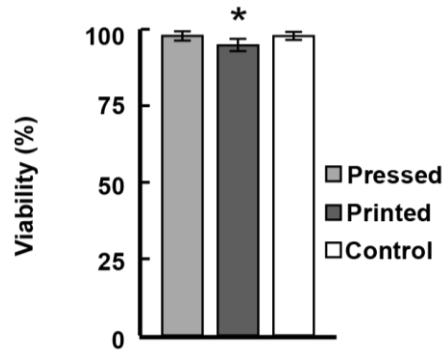


**Figure 5-1.** SMP MM4520 has good cytocompatibility on both substrate fabrication methods. A significant difference was found only for the substrates that were 3D printed compared to the TCPS control. (\*  $p < 0.05$ ; one-way ANOVA).

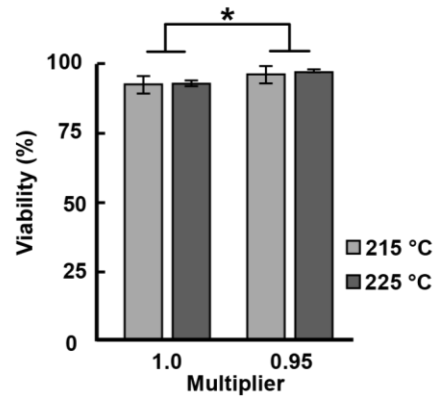


**Figure 5-2.** Multiplier affects viability of cells on 3D printed substrates. A lower multiplier led to a significant increase in viability at both temperature settings, but all printing parameter combinations showed high viability above 90%. (\*  $p < 0.05$ ; two-way ANOVA).

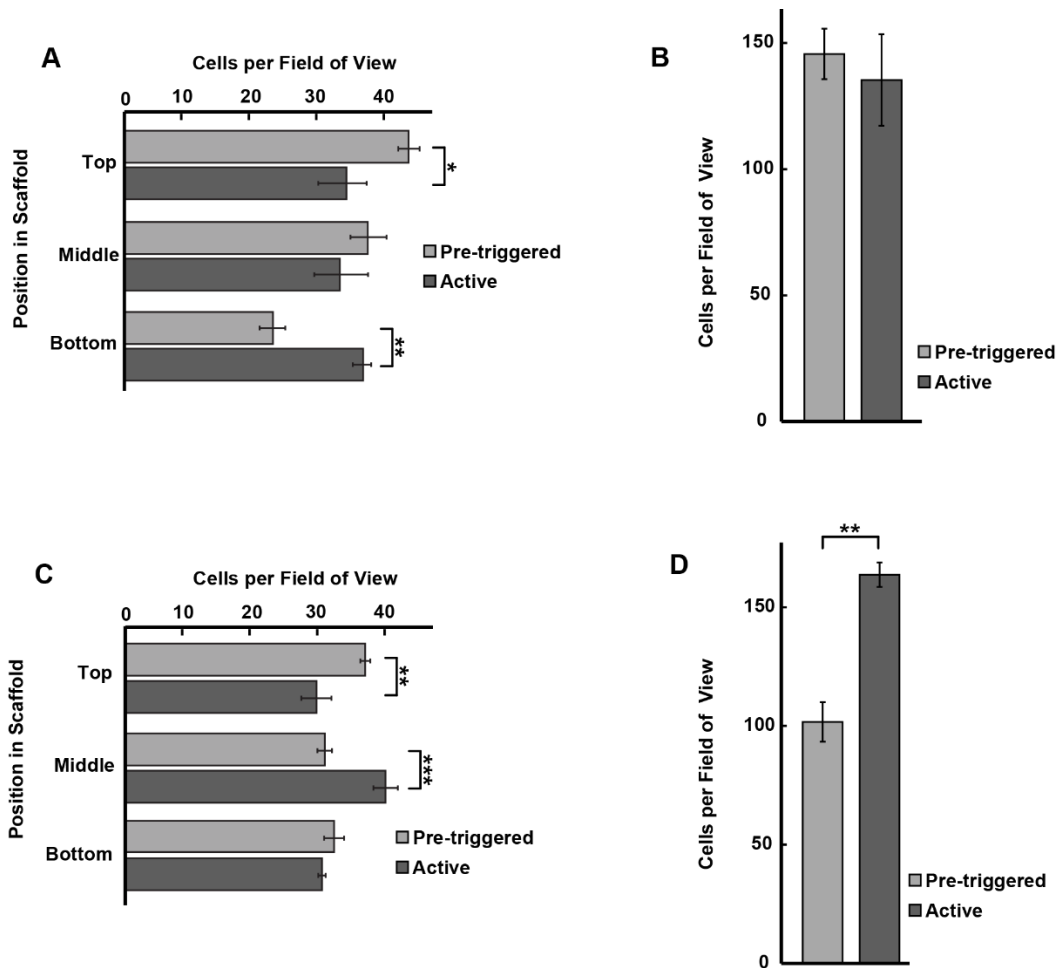


**Figure 5-3.** Cells present in the top, middle, and bottom thirds of (A) 40°C and (C) 70°C scaffolds with corresponding total cell per field of view (B) 40°C and (D) 70°C. (\*  $p < 0.05$ ; \*\*  $p < 0.01$ ; \*\*\*  $p < 0.001$ , Student's t-test).

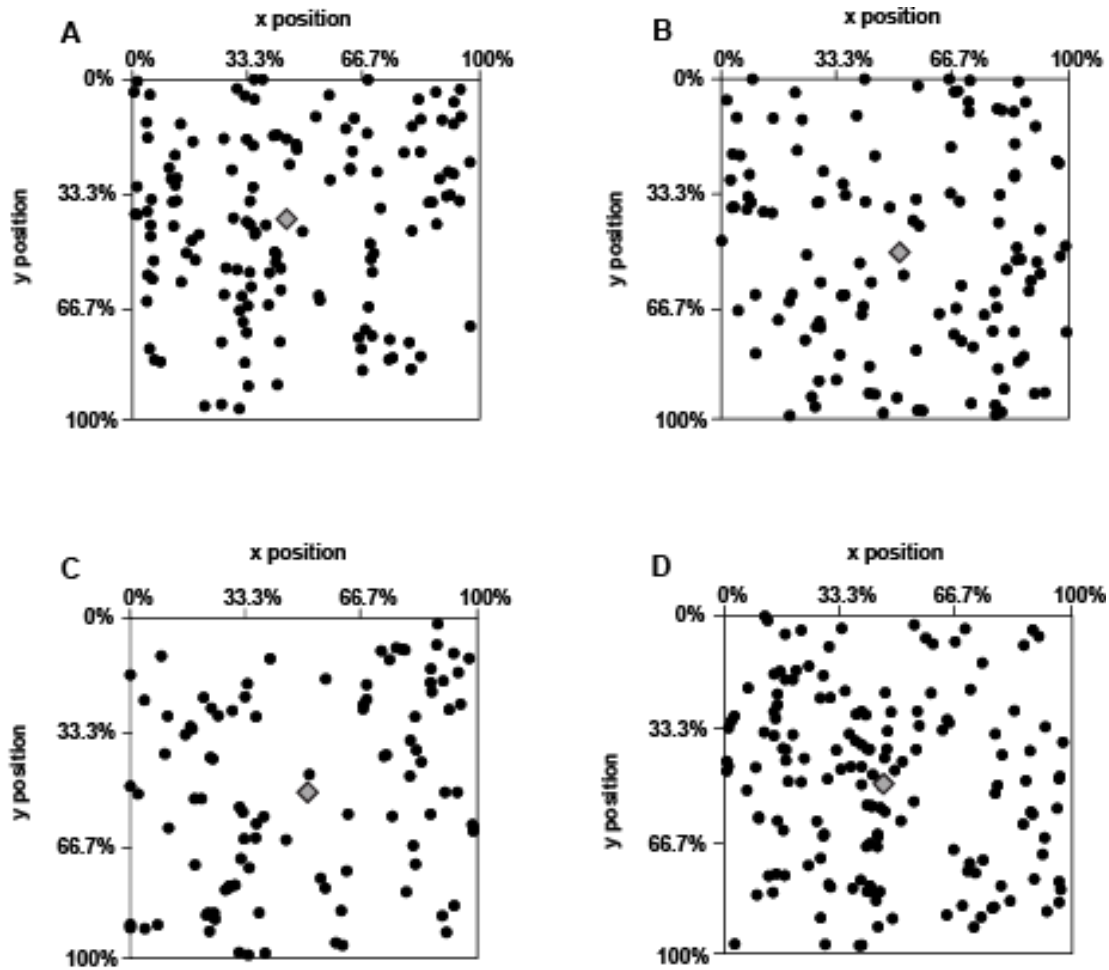


**Figure 5-4.** Representative figure of x position (from left) and y position (from top) of normalized cell distribution within cross section of (A) 40°C pre triggered (B) 40°C active, (C) 70°C pre-triggered and (D) 70°C active scaffolds. Diamond marker shows cell position centroid.

## 5.6 References

1. Ulery, B. D., Nair, L. S. & Laurencin, C. T. Biomedical applications of biodegradable polymers. *J. Polym. Sci. Part B Polym. Phys.* **49**, 832–864 (2011).
2. Zdrahala, R. J. & Zdrahala, I. J. Biomedical Applications of Polyurethanes: A Review of Past Promises, Present Realities, and a Vibrant Future. *J. Biomater. Appl.* **14**, 67–90 (1999).
3. Farè, S. *et al.* In vitro interaction of human fibroblasts and platelets with a shape-memory polyurethane. *J. Biomed. Mater. Res. - Part A* **73**, 1–11 (2005).
4. De Nardo, L. *et al.* Shape memory polymer foams for cerebral aneurysm reparation: Effects of plasma sterilization on physical properties and cytocompatibility. *Acta Biomater.* **5**, 1508–1518 (2009).
5. De Nardo, L. *et al.* Preparation and characterization of shape memory polymer scaffolds via solvent casting/particulate leaching. *J. Appl. Biomater. Funct. Mater.* **10**, 119–126 (2012).
6. Kapałczyńska, M. *et al.* 2D and 3D cell cultures - a comparison of different types of cancer cell cultures. *Arch. Med. Sci.* **14**, 910–919 (2018).
7. Bissell, M. J., Rizki, A. & Mian, I. S. Tissue architecture: the ultimate regulator of breast epithelial function. *Curr. Opin. Cell Biol.* **15**, 753–762 (2003).
8. Gilbert, P. M. *et al.* Substrate elasticity regulates skeletal muscle stem cell self-renewal in culture. *Science* **329**, 1078–1081 (2010).
9. Engler, A. J., Sen, S., Sweeney, H. L. & Discher, D. E. Matrix elasticity directs stem cell lineage specification. *Cell* **126**, 677–689 (2006).
10. Griffith, L. G. & Swartz, M. A. Capturing complex 3D tissue physiology in vitro. *Nat.*

- Rev. Mol. Cell Biol.* **7**, 211–224 (2006).
11. Cawkill, D. & Eaglestone, S. S. Evolution of cell-based reagent provision. *Drug Discov. Today* **12**, 820–825 (2007).
  12. Lee, J., Cuddihy, M. J. & Kotov, N. A. Three-dimensional cell culture matrices: state of the art. *Tissue Eng. Part B. Rev.* **14**, 61–86 (2008).
  13. Solchaga, L. A. *et al.* A rapid seeding technique for the assembly of large cell/scaffold composite constructs. *Tissue Eng.* **12**, 1851–1863 (2006).
  14. Merchuk, J. C. Shear effects on suspended cells. *Adv. Biochem. Eng. Biotechnol.* **44**, 65–95 (1991).
  15. Pei, M. *et al.* Bioreactors mediate the effectiveness of tissue engineering scaffolds. *FASEB J. Off. Publ. Fed. Am. Soc. Exp. Biol.* **16**, 1691–1694 (2002).
  16. Forster, B., Ville, D. V. A. N. D. E., Berent, J., Sage, D. & Unser, M. Complex Wavelets for Extended Depth-of-Field : A New Method for the Fusion of Multichannel Microscopy Images. **42**, 33–42 (2004).
  17. Schindelin, J. *et al.* Fiji: an open-source platform for biological-image analysis. *Nat. Methods* **9**, 676–682 (2012).
  18. Davis, K. A., Luo, X., Mather, P. T. & Henderson, J. H. Shape Memory Polymers for Active Cell Culture. *J. Vis. Exp.* 2–6 (2011) doi:10.3791/2903.
  19. Baker, R. M., Tseng, L.-F., Iannolo, M. T., Oest, M. E. & Henderson, J. H. Self-deploying shape memory polymer scaffolds for grafting and stabilizing complex bone defects: A mouse femoral segmental defect study. *Biomaterials* **76**, 388–398 (2016).
  20. Yu, K. & Qi, H. J. Temperature memory effect in amorphous shape memory polymers. *Soft Matter* **10**, 9423–9432 (2014).

21. Vunjak-Novakovic, G. *et al.* Dynamic cell seeding of polymer scaffolds for cartilage tissue engineering. *Biotechnol. Prog.* **14**, 193–202 (1998).

## **Chapter 6: Concluding Remarks and Future Work**

### **6.1 Overall Conclusions and Contributions**

The goal of this dissertation was to advance 4D printing in the biomedical field by utilizing a commercially available FDM printer and SMP to fill gaps in the understanding of how the printing process affects the shape memory behavior of SMPs and the extent to which strains could be programmed during the printing process to create ready-to-trigger SMP parts. In order to create robust SMP devices, it is critical to understand how printing parameters could potentially affect the ability of the device to function. Results from our studies can be expected to help further the utilization of high performing SMP devices in biomedical applications.

#### **6.1.1 Material Selection and Filament Fabrication**

In chapter 2, a method was developed for creating spools of 3D printer compatible filament from small quantities of SMP. We did this by repurposing a melt-spinner, which had been originally designed to spin PEEK fibers into a single strand<sup>1</sup>. The spooler on the device drew fibers out of a six-point die. We fabricated a single point die and used the plunger to push the SMP out of the die, in other words, we transitioned the melt-spinner into a small extruder. This was a reliable filament making method and is suitable for producing spools of custom made SMP materials in small quantities, which has implications in research labs.

Through this work we were also able to establish that SMP MM4520 is an appropriate SMP to use in 4D printing research. This material can be implemented in future research projects because of its availability and reliable performance during extrusion, printing, and cytocompatibility testing (*see 6.1.4*).

### **6.1.2 Printing Parameters Affect Key Properties of 4D Printed Shape Memory Polymers**

A major conclusion in this thesis is that printing parameters affect the shape memory behavior of the SMP. Specifically, as fiber orientation deviates from the programming axis, fixity decreases and recovery becomes more variable. This indicates that the print path is critical to SMP performance and, to achieve the greatest amount of fixing and recovery, should be in the direction of the intended programming. We also observed that raster printed edges contribute to the behavior of the SMPs, which is likely a product of the small cross-section of the dogbones. A scaled-up dogbone, with a wider cross-section, may behave more similarly to our punched samples.

### **6.1.3 Programming via Printing**

Our goal in chapter 4 was to quantify the extent to which strains can be trapped in an SMP part through the printing process. With the long-term goal of programming ready-to-trigger SMP parts during printing rather than following printing, this was a critical step to determine both the ability of the printer to trap strains in, and the recovery behavior of, 1D, 2D, and 3D samples. We successfully demonstrated that the FDM printing process can produce strains in SMP fibers. The degree to which strains can be trapped in SMP fibers is dependent on printing temperature, where lower temperatures trap higher strains. This concept was then applied to 3D structures, where we printed porous, self-contracting scaffolds that could be applied to *in vitro* applications.

### **6.1.4 Confirming Cytocompatibility and Utilizing PVP *in Vitro***

In chapter 5 we confirmed the cytocompatibility of the commercially available SMP MM4520, which supports its future use as an easily obtainable and printable SMP for biomedical applications. Furthermore, we showed that the SMP has good viability under different printing conditions and that implementing a lower multiplier, which decreases fiber diameter, can

potentially create microenvironments within the substrate, which contribute to increased cell viability.

PvP cell scaffolds were used as active 3D cell culture platforms to present an *in vitro* application of a self-contracting SMP part. The printing parameters for the scaffold were realized through our results from chapter 4. Here, we successfully demonstrated using PvP as a means to increase the cell distribution through a 3D porous scaffold.

## 6.2 Recommendations for Future Work

In this dissertation, we used a commercially available shape memory thermoplastic polyurethane, SMP MM4520. While this SMP met our selection criteria for printing and processing and has been successful in the 4D printing and biomedical literature<sup>2-4</sup>, an SMP with a transition temperature closer to cell culture conditions may be more beneficial for future, biomedical, PvP studies. The manufacturer of SMP MM4520, SMP Technologies Inc., also synthesizes an SMP with a  $T_g$  of 35°C. Because the transition temperature is closer to body temperature, it could exhibit greater strain release when triggering *in vitro*, thus creating a more pronounced contraction in PvP active cell culture platforms.

The study in chapter 3 revealed that fiber orientation affects both the fixity and recovery of a 4D printed SMP. This could be further studied with additional samples printed with a combination of fiber orientations (e.g., a dogbone with fiber orientation alternating by layer), to determine the extent to which a more complex print path could affect shape memory behavior. Additionally, as previously mentioned, a geometry with a greater cross-sectional area could be studied for the effects of the raster-printed edges.

The development of PvP in this dissertation provides exciting opportunities for future study. In the work presented, we studied a constant strain (i.e., no gradient) with varying pore

sizes. A future experiment could program a strain gradient using different printing temperatures at various points in the printing process. Additionally, the modeling could be added upon to include the anisotropic material properties, and more studies could be performed to explore quantify trapped strain with relation to printing thickness. At the cellular level, it could be beneficial to fabricate a PVP scaffold with a smaller, more cell-relevant pore size<sup>5,6</sup>. Our study was limited to the macroscopic regime by the resolution of the printer (200  $\mu\text{m}$ ), however, the similar methods described in chapter 4 could be followed using a printer with higher resolution. Finally, 3D printers can print objects from medical imaging data (e.g., CT, MRI), which enables the fabrication of highly tailored devices. For example, a self-tightening custom bone cast or self-expanding personalized stents<sup>7,8</sup>. Overall, the PVP process developed in this work can be anticipated to enable new strategies in personalized medicine, cellular research platforms, and elsewhere in the biomedical field.

## 6.2 References

1. Ouellette, E. S. Novel Methods and Self-Reinforced Composite Materials for Assessment and Prevention of Mechanically Assisted Corrosion in Modular Tapers. (2016).
2. Yang, Y., Chen, Y., Wei, Y. & Li, Y. 3D printing of shape memory polymer for functional part fabrication. *Int. J. Adv. Manuf. Technol.* **84**, 2079–2095 (2016).
3. Garcia Rosales, C. A. *et al.* Characterization of shape memory polymer parts fabricated using material extrusion 3D printing technique. *Rapid Prototyp. J.* **25**, 322–331 (2019).
4. Abuzaid, W., Alkhader, M. & Omari, M. Experimental analysis of heterogeneous shape recovery in 4d printed honeycomb structures. *Polym. Test.* **68**, 100–109 (2018).
5. Huang, G. *et al.* Functional and Biomimetic Materials for Engineering of the Three-

- Dimensional Cell Microenvironment. *Chem. Rev.* **117**, 12764–12850 (2017).
6. Walker, G. M., Zeringue, H. C. & Beebe, D. J. Microenvironment design considerations for cellular scale studies. *Lab Chip* **4**, 91–97 (2004).
  7. Bodaghi, M., Damanpack, A. R. & Liao, W. H. Self-expanding / shrinking structures by 4D printing. (2016).
  8. Baker, R. M., Tseng, L.-F., Iannolo, M. T., Oest, M. E. & Henderson, J. H. Self-deploying shape memory polymer scaffolds for grafting and stabilizing complex bone defects: A mouse femoral segmental defect study. *Biomaterials* **76**, 388–398 (2016).

## VITA

**NAME OF AUTHOR:** Kathleen Pieri

**PLACE OF BIRTH:** Syracuse NY, USA

**DATE OF BIRTH:** November 22, 1993

### EDUCATION:

B.S. in Bioengineering, Syracuse University, 2016

PhD. in Bioengineering, Syracuse University, 2016 – present

### PUBLICATIONS AND PRESENTATIONS:

**Pieri, K.**, Felix, B., Soman, P., Henderson, J. H. “Printing Parameters Affect 4D Printed Shape Memory Polymers.” In Preparation.

**Pieri, K.**, Chando, P., Soman, P., Zhang, T., Henderson, J. H. “Programming via 4D Printing to Advance Shape Memory Polymers in Biomedical Applications.” In Preparation.

Felix, B., **Pieri, K.**, Henderson, J.H. “3D Printing Shape Memory Polymers.” 2019. Syracuse Summer Research Symposium. Syracuse University. (Poster)

Hart, E. K., Jannini, A.V. S., Johnson, A. J., **Pieri, K.** “Forming Key Partnerships to Enhance Graduate Student Programming.” *American Society for Engineering Education*. 2019.

**Pieri, K.**, Chando, P., Soman, P., Henderson, J. H. “Programming via Printing: Printing Ready-to-Trigger, Biocompatible, Shape-Memory Polymers.” 2019. Society for Biomaterials, Annual Meeting. Seattle, Washington. (Poster)

**Pieri, K.**, Chando, P., Soman, P., Henderson, J. H. “Programming via Printing: Printing Ready-to-Trigger, Biocompatible, Shape-Memory Polymers.” 2019. Stevenson Biomaterials Research Day. Syracuse University. (Poster)

Sivan, S., **Pieri, K.**, Gilbert, J.L. “Cell-Induced Corrosion on Titanium Alloys.” 2015. Orthopedic Research Society, Annual Meeting. Las Vegas, Nevada. (Poster)